Flexible Packaging for a Wireless Intraocular Pressure Sensor

Çağdaş Varel

A dissertation
submitted in partial fulfillment of the
requirements for the degree of

Doctor of Philosophy

University of Washington

2013

Reading Committee:
Karl F. Böhringer, Chair

Lih-Yuan Lin

Brian Otis

Program Authorized to Offer Degree:
Electrical Engineering

©Copyright 2013

Çağdaş Varel

University of Washington

Abstract

Flexible Packaging for a Wireless Intraocular Pressure Sensor

Çağdaş Varel

Chair of the Supervisory Committee:

Professor Karl F. Böhringer

Electrical Engineering

This dissertation focuses on the prototype of an intraocular pressure (IOP) sensor as a major step towards building a device that can be permanently implanted during cataract surgery. The implantation will proceed through an incision of 2-3 mm using an injector, during which the complete device must be folded into a cross-section of 2 mm × 1 mm. The device uses radio frequency (RF) for wireless power and data transfer.

First, a novel device design is introduced. Materials are chosen systematically for the device fabrication. Two fabrication methods, metal-on-elastomer and solder-filled microchannel, are tested for the antenna fabrication and device integration. Results indicate that an antenna resistance below 5 Ω can be achieved using the solder-filled microchannel method. A device fabrication and integration process based on that method is introduced.

A device prototype including an antenna, an RF chip and a pressure sensor is presented. It is assembled on a printed circuit board (PCB) with several circuit components used for testing and

calibration. The antenna is fabricated and integrated with the circuit using a fabrication method employing solder-filled microchannels embedded in an elastomer (polydimethylsiloxane, PDMS). The presented method can be used for biocompatible packaging of microsystems and sensors.

The prototype is tested for antenna functionality through power and data transfer. The monitoring device is powered at 2.716 GHz from a distance of 1-2 cm. Transferred power is greater than the threshold power required for chip operation. Exposure to RF power is kept below the maximum permissible exposure limit. The backscattered signal is observed in each chip mode to confirm the wireless sensing capability.

Structural flexibility of the PDMS-metal-PDMS stack is studied using a mockup device. The effect of applied stress on antenna resistance is monitored in order to evaluate its durability during the implantation process. The flexible antenna can withstand a stress of 33.4 kPa without any electrical disconnection. It did not show a significant increase in electrical resistance after 50 bending cycles.

The prototype has undergone electrical tests for the effect of PDMS coating on pressure sensor and wireless sensing performance. An acceptable increase in sensor capacitance and pressure sensitivity is observed after PDMS coating. Wireless pressure measurement tests showed device operation with a pressure sensitivity of 16.66 Hz/mm-Hg (0.125 Hz/Pa).

Three topics for future work are proposed for converting the prototype into a complete device. First, additional tests for evaluating device performance in an eye-like environment are proposed. They provide a complete characterization of the RF power and data transfer inside the eye. Second, requirements for the next generation of RF chip are stated. Device size will be shrunk by the elimination of surface mount technology (SMT) components and PCB. Third, building a multi-sensor platform based on the prototype is proposed. Salinity and pH sensors can be added

to the prototype.

TABLE OF CONTENTS

Page

LIST OF FIGURES iii
LIST OF TABLES vi
CHAPTER 1. Introduction 1
CHAPTER 2. Flexible Packaging Method for an Intraocular Pressure Sensor Implanted during a Cataract Surgery 5
2.1 Introduction 5
2.2 Packaging Material 7
2.3 Fabrication Method 8
2.3.1 Metal-on-Elastomer 9
2.3.2 Solder-Filled Microchannel 16
2.3.3 Comparison of Fabrication Methods 20
2.4 Integration Scheme 20
2.5 Compatibility with PEU Ring 23
2.6 Conclusion 24
CHAPTER 3. Prototype of the Intraocular Pressure Monitoring Device 25
3.1 Introduction 25
3.2 Device Prototype 25
3.3 Prototype Fabrication 26
3.3.1 Parts and Part Assembly 26
3.3.2 Antenna Fabrication and Integration 27
3.3.3 Fabrication Results 29
3.4 Conclusion 30
CHAPTER 4. Solder-filled Microchannel Antenna Performance 31
4.1 Introduction 31
4.2 RF Power Transfer 31
4.3 RF Exposure Limit 33

4.4 Transmission of Measurement Results 34
4.5 Conclusion..35
CHAPTER 5. Mechanical Properties of the Solder-filled Antenna Structure...............................36
5.1 Introduction 36
5.2 Mockup Device 36
5.3 Measurement Setup 37
5.4 Results..38
5.5 Conclusion...41
CHAPTER 6. Pressure Measurement...42
6.1 Introduction 42
6.2 Effect of PDMS Coating on Pressure Sensor 42
6.3 Wireless Pressure Measurement...44
6.4 Conclusion...47
CHAPTER 7. Conclusions and Future Work 48
7.1 Conclusions 48
7.2 Future Work 49
7.2.1 Testing in an Eye Model 49
7.2.2 From Prototype to a Complete Device..49
7.2.3 Salinity and pH Monitoring 49
References ……………………………………………………………………………..52

LIST OF FIGURES

Figure 2.1: Capsular tension ring and the implant location. a) Schematic view of the anterior segment of the eye (courtesy of National Eye Institute). The implant will be placed in the lens capsule. b) Commercially available lens-ring pair implanted in the eye (courtesy of StabilEyes^{TM}). 5

Figure 2.2: A complete device embedded in a tension ring-like PEU enclosure. 6

Figure 2.3: Fabrication steps for the metal-on-elastomer. Cross-sectional view along A-A' is illustrated. a) Metal patterning on glass substrate by lift-off, b) PDMS spin-coating and curing, c) Metal transfer after peeling PDMS from glass, d) Laser cutting for the ring shape, e) Solder dip-coating and chip assembly. 9

Figure 2.4: Circular metal pattern on PDMS after transfer. Close-up view shows irregular waves on the metal surface profile. 10

Figure 2.5: Wavy metal structure due to the thermal expansion coefficient mismatch. Surface profile of the metal along the dotted line is plotted. The amplitude of the wave has an irregular characteristic. The peak-to-peak amplitude of the wave can reach up to 2 μm. 12

Figure 2.6: Metal-on-elastomer patterns are observed during the fabrication process for buckling. No visible change is observed in steps a) and b). Buckling is presented after peeling at room temperature in step c). 13

Figure 2.7: Effect of cooling process on buckling: a) Substrate is heated and cooled rapidly. Buckling is more vigorous. b) Heating and cooling is performed gradually resulting in smoothed waves. 13

Figure 2.8: Left: Assembled device (actual chips replaced with SMT devices with dimensions similar to the chips for testing the packaging method). Right: Illuminated LED showing the conductivity of the metal pattern. 14

Figure 2.9: The Cr/Au layer is evaporated on PDMS through a Si shadow mask. 15

Figure 2.10: Metal-on-PDMS structures made with shadow masking. The metal surface is much smoother compared to the previous fabrication method. 16

Figure 2.11: Fabrication process for a ring antenna. Cross-section along the connection pads, A-A', is illustrated. a) SU-8 mold on Si wafer for PDMS shaping. b) PDMS is

spin-coated on the mold and polymerized. c) The microchannel is formed by PDMS-to-PDMS bonding via O_2 plasma. d) The channel is filled with MPTMS solution, within 10 minutes of the plasma treatment, in order to increase wettability by solder, and left for drying. e) Sample is heated to 75^0C and a drop of solder (51% In 32.5% Bi 16.5% Sn alloy) is delivered to the inlet. 18

Figure 2.12: Microscope view of the ring antenna from three different regions. 19

Figure 2.13: Defects observed in the solder-filled microchannels. a, b) Trapped air or surface treatment agent in the microchannel causes a gap or cavity in the metal. c) Top surface of the channel collapsed during PDMS bonding. This resulted in a defect in the metal. 19

Figure 2.14: Heat-assisted repair of a break in the antenna: a) metal pattern embedded in PDMS before breaking; b) broken metal pattern; c) repaired metal pattern. 20

Figure 2.15: Illustration of the device without the PDMS structure and the tension ring. a) The general view including the ring antenna and the chips. b) The close-up view of three interconnections. Each of them requires two inlets for the fabrication. 22

Figure 2.16: The mold, made of Si, for the PDMS structure and the chips to be integrated. Red pillars represent SU-8 structures for immobilizing the chips. 23

Figure 3.1: Illustration of the prototype device. Chip, sensor and circuit components are first assembled on a PCB, and then embedded in PDMS for antenna fabrication. 25

Figure 3.2: PCB layout of the prototype. PS: Pressure sensor; R1,R2, R3: SMT resistors; C1,C2, C3: SMT capacitors; L1: SMT inductor. 27

Figure 3.3: The pattern for the SU-8 mold. Thinner lines indicate the laser cutting locations. The inner region of the PDMS is cut out in order to access the PCB. 28

Figure 3.4: Schematic view of the fabrication process for the antenna-PCB integration. Cross-section is along A-A'. 29

Figure 3.5: Antenna and PCB interconnected and embedded in PDMS. The top surface of PDMS is cut in order to get access to the board. The close-up views show that the ring-shaped metal structure does not have defects. 30

Figure 4.1: Test setup for RF power transfer to the prototype. 31

Figure 4.2: Power transferred to the chip at various transmitted power levels and transmission distance. 32

Figure 4.3: 2-turn and 3-turn solder-filled microchannels that can be used as an antenna............33

Figure 4.4: Test setup for data transmission from the device. 34

Figure 4.5: Frequency spectrum of the backscattered signal in three measurement modes, at room temperature and atmospheric pressure. 35

Figure 5.1: Fabrication process for the mockup device. a) SU-8-on-Si mold; b) PDMS spin-coating on the mold; c) SMT components on a Si wafer; d) PDMS coating on SMT components and peeling from the wafer; e) PDMS-to-PDMS bonding upon O_2 plasma treatment; f) surface treatment on the microchannel surface; g) solder delivery. 36

Figure 5.2: Illustration of the test setup. A point load is applied at the edge of the PDMS while bending is observed with a camera and resistance change is observed with a multimeter. 38

Figure 5.3: The antenna in the mockup device is tested for its electrical conductivity under mechanical stress. The stress is applied in steps while the antenna resistance and the amount of displacement are monitored. 39

Figure 5.4: Resistance change in solder-filled antenna pattern with applied stress. 40

Figure 5.5: The change in antenna resistance after bending the device 50 times. 40

Figure 5.6: Histogram of the antenna resistance measured over 150 bending cycles. 41

Figure 6.1: Pressure sensor reading before and after PDMS coating. Error bars show the uncertainty in capacitance due to LCR meter.. 43

Figure 6.2: Amount of change in pressure sensor capacitance with PDMS coating. 43

Figure 6.3: Test setup for the wireless pressure measurement. 44

Figure 6.4: Above: Change in Δf_P with increased pressure. Below: Frequency spectrum for each data point...45

Figure 7.1: Setup used for salinity and pH measurements, and its circuit representation. R_e: resistance due to the redox reactions on the electrodes. R_w: resistance of the solution. C_{dl}: capacitance due to the double layer formation around the electrodes. 50

Figure 7.2: Change in solution resistance with NaCl concentration. pH is kept constant in this measurement. 51

Figure 7.3: Change in solution resistance due to change in pH and NaCl concentration. 51

LIST OF TABLES

Table 1.1: Selected works on IOP sensors. (Cap.: Capacitive, Piezo.: Piezoresistive, Ind.: Inductive, IOL: Intraocular Lens) 2

Table 2.1: Comparison of PDMS, parylene-C and polyimide as a biocompatible and flexible packaging material. 8

Table 2.2: Comparison of theoretical and experimental electrical conductivity among different batches, before and after transfer to PDMS. 15

Table 2.3: Commercially available low temperature solders (data from Indium Corp.)................17

Table 3.1: Connection pads on PCB and their function. 27

ACKNOWLEDGMENTS

Writing this thesis would not be possible without the help and support of great people in the Electrical Engineering Department and Micro Fabrication Facility. Prof. Karl F. Böhringer, my thesis advisor and committee chair, has provided me vision, guidance and optimism throughout my research. I am very grateful for our valuable conversations despite his many academic and professional commitments. I would like to thank Prof. Brian Otis, Prof. Tueng T. Shen, Prof. Buddy Ratner, Yi-Chun Shih and Felix Simonovsky for their valuable ideas and support.

I would also like to present my gratitude to the following people for their continuous help and support:

- Past and present members of the MEMS group, especially Yegan Erdem, Shaghayegh Abbasi, Ji Hao Hoo and Kwang Soon Park, who have kept me in good company during my graduate studies.
- My parents for always supporting me.
- Gozde Durmus, Ozlem Arat and Valerie Lieu, whose friendship I will always remember.

This work was supported in part by the Coulter Foundation and by the John M. Fluke Endowment to the University of Washington. Part of this work was conducted at the University of Washington Microfabrication / Nanotechnology User Facility, a member of the NSF National Nanotechnology Infrastructure Network.

CHAPTER 1. INTRODUCTION

Glaucoma is the second leading cause of blindness globally after cataract, according to the World Health Organization [1]. In 2010, 8.4 million people were blinded because of glaucoma [2]. This is estimated to rise to 11.2 million by 2020. Glaucoma is a disease in which the damage in the optical nerve causes visual field loss and ultimately blindness. Increase in the intraocular pressure (IOP) is considered to be one of the factors causing glaucoma, along with genetic reasons. Therefore, IOP levels are monitored as a clinical parameter to diagnose glaucoma. Intraocular pressure (IOP) is the fluid pressure of the aqueous humor inside the eye. An increase in IOP occurs due to malfunction in the drainage network. IOP over 21 mmHg can cause an optical nerve damage and, eventually, blindness. This limit can vary among people. The loss of vision progresses over a long time period without any significant pain in open-angle glaucoma, which accounts for 90% of cases in USA. Thus, it is unnoticeable to the patient until the loss of vision is significant and irreversible. Ocular tonometry is used to determine the IOP conventionally. Since this procedure requires a visit to the clinic and local anesthesia on the cornea, IOP measurements are generally taken with intervals of several months. IOP can also vary during the day depending on the patient's activity [3]. The conventional measurement method does not have 24-hour monitoring capability for fluctuations in IOP. More frequent measurements and 24-hour monitoring capability are required in order to capture the fluctuations in IOP levels more rapidly. This will enable the early diagnosis of glaucoma, before irreversible nerve damage, and provide insight to progress of the disease.

The miniaturization trend in sensors and electronics presents new opportunities for continuous monitoring of IOP and diagnosis of glaucoma in an early stage. Researchers noticing this opportunity have presented IOP monitoring devices, which can be embedded in an intraocular lens (IOL) like structure [4-6], implanted in the anterior chamber [7-9], penetrating into the eyeball through a needle [10] or embedded in a contact lens [11, 12]. Devices that use telemetry for wireless transmission suffer from limited range of transmission while active devices require a battery. An intermediate solution can be employing low-power active circuits that are powered wirelessly [13].

A MEMS pressure sensor equipped with a low-power radio frequency (RF) chip is a promising tool to perform continuous IOP monitoring. Such a device can keep track of the pressure and transmit the information to an outside receiver. Then, the receiver can process and store the data and notify the physicians about the trend of the IOP daily. A typical device would employ an RF chip, pressure sensor and an antenna. Numerous groups have worked on an IOP monitoring device. Those platforms diversify depending on the power/data transmission method, packaging,

implantation location and pressure sensor technique, as presented in Table 1.1. It is seen that capacitive pressure sensing is preferred in various cases due to its low-power operation and sensitivity. For the data transmission method, there is a competition between active chips and passive circuits. An active chip can provide a better transmission range while requiring more power compared to a passive circuit. However, a passive circuit has a limited transmission distance.

Table 1.1: Selected works on IOP sensors. (Cap.: Capacitive, Piezo.: Piezoresistive, Ind.: Inductive, IOL: Intraocular Lens)

No.	University	Sensing Method	Data Transmission	Packaging Material	Implant Location	Size (mm)	Ref.
1	Uppsala University	Cap.	Passive	Silicone	IOL	3 × 3 × 1	[4]
2	RWTH Aachen	Cap.	Active	Silicone	IOL	2.6 × 2.6	[5, 6]
3	UIUC	Piezo.	Wired	N/A	N/A	9 × 9 × 0.5	[14, 15]
4	EPFL	Strain gauge	Wired / Active	Silicone	Contact Lens	7.1 (radius)	[11, 12]
5	Caltech	Bourdon tube	Passive (Optical)	Parylene	Anterior chamber	1 (radius)	[16]
6	Caltech	Cap. / Cap. & Ind.	Passive	Parylene	Anterior chamber	4 × 2	[8]
7	Caltech	Cap.	Passive	Parylene	Anterior chamber	4 × 1.5 × 1	[17]
8	Michigan	Cap.	Active	Glass	Anterior chamber	1.5 × 2 × 0.5	[9]
9	UW	Cap.	Active (RF powered)	PDMS/PEU	Anterior chamber	6.5 (radius)	

Recently, Leonardi et al. proposed a contact lens-based, non-invasive device, where a strain gauge is used to measure the curvature of the cornea [18]. The device is promising since it does not require

any surgery. However, it performs an indirect measurement of IOP and its accuracy is affected from the variation of the cornea thickness and diameter. In contrast to that, intraocular devices can perform direct pressure measurements. But, they require surgery for device implantation. Chen et al. demonstrated a parylene-based implantable IOP sensor [17]. Their device uses a capacitive pressure sensor transmitting the measurement results with passive telemetry. This makes the device more susceptible to noise compared to an active RF chip and limits its transmission distance. Other notable work in the literature employs a similar approach with active or passive telemetry [4, 5, 19].

There has been a tremendous effort in developing an implantable IOP monitoring device as seen in the literature. However, they fail to address the device implantation problem, which is a serious concern for any implantable device limiting its usage. Aforementioned devices require surgery for the device implantation except the contact lens device. This requirement prevents the wide acceptance of those devices since patients are reluctant to undergo a surgery for a disease they have not suffered yet. Unless an anomaly is recognized in IOP levels, a potential patient will not be aware of the risk until glaucoma symptoms are apparent. And in that stage, an IOP monitoring device will have limited use since vision loss has already occurred. Integration of the IOP monitoring device with existing, well-established implant designs and surgery procedures is critical for its acceptance. The IOP monitoring device presented in this thesis is designed to be embedded into a capsular tension ring-like structure, an apparatus implanted in cataract surgery. The monitoring device is fabricated by the assembly of a capacitive pressure sensor, RF circuit chip and a loop antenna. It is first enclosed in a polymethylsiloxane (PDMS) structure and later embedded into a poly-(ether urethane) (PEU) ring.

Chapter 2 introduces a novel IOP sensor platform design tailored to be compatible with the suture-less cataract surgery. Two fabrication methods, metal-on-elastomer and solder-filled microchannels, are investigated for the proposed flexible structure. Preliminary results for both methods are presented. The solder-filled microchannel method is chosen for antenna fabrication and device packaging. The self-healing aspect of the method is also investigated for the antenna.

Chapter 3 details the fabrication of the first generation IOP monitoring device. The device incorporates the sensor and the RF chip on a printed circuit board while the antenna is assembled with the board using solder-filled microchannels. The whole system is packaged within a flexible structure. However, overall flexibility is currently limited by the printed circuit board. Results from on-the-bench tests are presented.

Chapter 4 analyzes the antenna performance of the solder-filled microchannel. Two sets of tests are performed in order to investigate the power and data transmission using the antenna.

Chapter 5 presents the mechanical properties of the solder-filled antenna structure. A mockup

IOP monitoring device is fabricated using surface-mount technology (SMT) resistors integrated with an antenna. It is put under mechanical stress using a point load. It is seen that the structure can survive a mechanical stress of 116 kPa.

Chapter 6 shows the pressure sensor functionality of the device. A standalone pressure sensor is first tested for the effect of the elastomer coating on its performance. Later, an integrated device is tested for the wireless pressure measurement capability. A custom made pressure chamber is prepared for the relative pressure. The wireless pressure measurement method has a sensitivity of 16.66 Hz/mm-Hg.

Chapter 7 summarizes the work done thus far, and also details potential future work.

CHAPTER 2. FLEXIBLE PACKAGING METHOD FOR AN INTRAOCULAR PRESSURE SENSOR IMPLANTED DURING A CATARACT SURGERY

2.1 Introduction

The IOP monitoring device presented here is designed to be embedded into a capsular tension ring-like structure and implanted into the anterior chamber during cataract surgery (Figure 2.1). Cataract surgery has wide acceptance as a sutureless surgery and high demand due to cataract's prevalence. Modern cataract surgery methodology uses an incision of 2-3 mm. With microincision techniques, it can be decreased to 1.6 mm [20]. Furthermore, there are 22 million cataract patients over the age of 40 and 3 million surgeries performed each year in the USA. There is no concrete relationship between occurrence of cataract and glaucoma except that IOP increase is reported after cataract surgery in some cases [21]. However, both cataract and glaucoma are observed more often in an older population, after the age of 40. Thus, an IOP monitoring device implanted during cataract surgery will help early diagnosis of glaucoma in this part of the population. The beneficiaries of such a device can be calculated as 300,000 patients from a glaucoma occurrence rate of 1% at an age of 40.

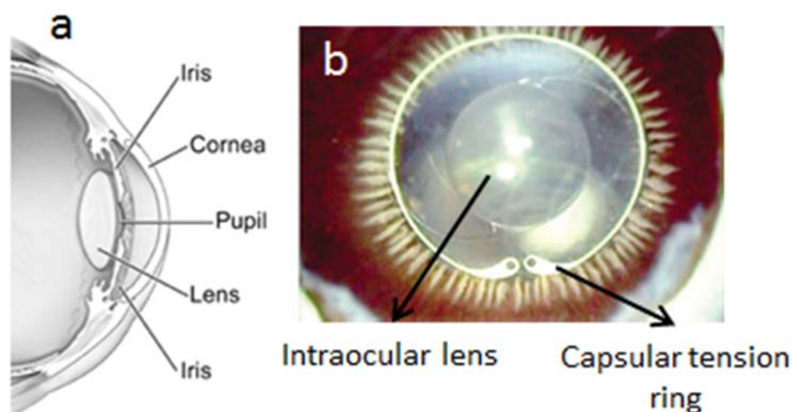

Figure 2.1: Capsular tension ring and the implant location. a) Schematic view of the anterior segment of the eye (courtesy of National Eye Institute). The implant will be placed in the lens capsule. b) Commercially available lens-ring pair implanted in the eye (courtesy of StabilEyes™).

The IOP monitoring device consists of a pressure sensor for physical measurements, an RF chip, and an antenna for power and data transmission as illustrated in Figure 2.2. The geometry of the

device is determined by the tension ring-like structure since it will be the final enclosure. This structure is made of PEU and has the shape of a torus with a major radius of 5.75 mm and a minor radius of 1.3-1.4 mm. The ring will be folded or squeezed and dried at an elevated temperature in order to keep its compressed state prior to surgery. It also has a shape-memory property which can be controlled with its water content. It will be placed into an injector to pass through an incision of 2-3 mm in length. The ring recovers to its original torus shape upon implantation because of an increase in water content. Flexibility of the embedded structure is critical considering the implantation process, compression and decompression steps. Design steps for the flexible package and details of the antenna fabrication process will be presented in this chapter along with the initial fabrication results.

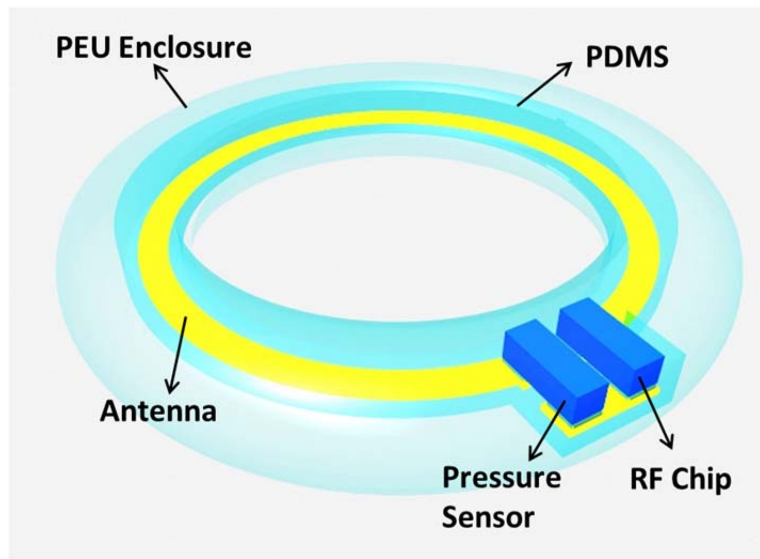

Figure 2.2: A complete device embedded in a tension ring-like PEU enclosure.

Two fabrication methods, metal-on-elastomer and solder-filled-microchannel, are studied for antenna fabrication and packaging. Metal-on-elastomer technique is first employed for fabrication of a loop antenna and electrical connection between chips. Preliminary results showed that performance and durability of the fabricated structures remain an issue. The presented flexible packaging method for a wireless intraocular pressure sensor is based on a novel and simple fabrication method employing a solder-filled-microchannel, which is discussed later in this chapter. Siege et al. introduced that method for co-fabrication of metallic and microfluidic structures in lab-on-chip devices [22-24]. Later, the solder-filled-microchannel method was used for fabrication of stretchable micro-needle arrays [25] and contact sensors [26]. The comparison

of solder-filled-microchannel and metal-on-elastomer methods is presented for the antenna fabrication.

The packaging discussed here considers an intermediate package of the antenna and chips until the device is embedded into the PEU ring. The PEU layer will be the final package for the complete device. Design steps for the flexible package include:

- Packaging material
- Fabrication method for the antenna and electrical interconnections
- Integration scheme for the chips and the antenna

2.2 Packaging Material

Packaging material is also designated as the substrate for the antenna and interconnects. Various polymers used in MEMS and flexible electronics have been considered for the packaging material. Polydimethylsiloxane (PDMS) is the most favorable candidate among them for several reasons. It is a chemically inert material and known in the bio-MEMS community for its biocompatibility. Moreover, PDMS is in the family of silicones and its Young's modulus varies between 360 and 870 kPa according to the mixing ratio of its ingredients, making it a stretchable material [27]. PDMS is used extensively in the field of microfluidics and many methods have been developed in order to fabricate various devices or tailor its physical properties. A comparison of PDMS with parylene-C and polyimide, two common polymers in flexible electronics, is presented in Table 2.1. Parylene-C is a transparent coating for BioMEMS sensors. It is biocompatible and resistant to processing chemicals used in microfabrication. It is deposited and patterned with conventional fabrication methods such as chemical vapor deposition (CVD) and oxygen plasma etching. Metal can be evaporated onto parylene-C and patterned with photolithography. Its pinhole-free deposition provides excellent sealing. Parylene-C is generally utilized as an added thin film, with thicknesses from few to tens of μm [28]. It is also gaining importance as a structural material [29, 30]. Polyimide is used commonly in the electronics industry as a passivation layer and for making flexible cables. It is a thermally stable polymer with structural flexibility and good chemical resistance. Its low toxicity and long term stability has been demonstrated but it is not certified as a biocompatible implant material [31-33]. Polyimide can be patterned by spin-coating, wet etching and oxygen plasma etching. There are also photodefinable polyimides. Metal can be evaporated onto polyimide and patterned with photolithography. Both polyimide and parylene-C have higher Young's moduli compared to PDMS. Both materials are exposed to chemicals during the photolithography process used for metal patterning. That can be a limiting factor for the long term low-toxicity since parylene-C and polyimide have moisture absorption rates of 0.06% and

0.8-1.4% respectively [31].

A PDMS structure can be easily embedded in the PEU tension ring since it does not require any changes in the ring fabrication method. Moreover, it does not alternate the shape-memory capability of the PEU ring. A simple experiment is performed to validate its compatibility with the PEU ring fabrication and to quantify its effect on the water-induced shape memory property (Chapter 2.5).

The embedded device is illustrated in Figure 2.2. As seen in the illustration, the antenna, interconnections and chips are first covered in a PDMS package and later embedded in the PEU tension ring. The PDMS package serves both as a protecting layer for the metal layers and as the only layer supporting the device before embedding it into the tension ring.

Table 2.1: Comparison of PDMS, parylene-C and polyimide as a biocompatible and flexible packaging material.

Material	Fabrication Process	Biocompatible	Young's Modulus (MPa)	Elongation (%)	References
PDMS	Spin-coating and molding	USP* Class VI	< 0.9	600	[27, 34-36]
Parylene-C	CVD and O_2 plasma	USP* Class VI	20	200	[28, 29, 37-39]
Polyimide	Spin-coating, photodefinable, wet etching and O_2 plasma	-	8830	30	[31, 40, 41]

*: United States Pharmacopeia

2.3 Fabrication Method

In the preliminary stage, methods for building flexible circuits are investigated for antenna fabrication and device packaging. Two fabrication methods, metal-on-elastomer and solder-filled microchannel, are selected among many flexible circuit technologies due to their biocompatibility, high flexibility due to PDMS nature, relatively simple fabrication and chip integration process. Flexible metal patterns fabricated with these two methods are compared. Parylene-C and polyimide based flexible circuit technologies are also considered. However, they are not chosen

for this application due to disadvantages presented in the previous section.

2.3.1 Metal-on-Elastomer

PDMS is the elastomer used in the metal-on-elastomer method. Two deposition methods are used in order to fabricate a metal pattern on PDMS. The first method employed metal transfer from a handling glass wafer while the metal layer is deposited through a shadow mask in the second method.

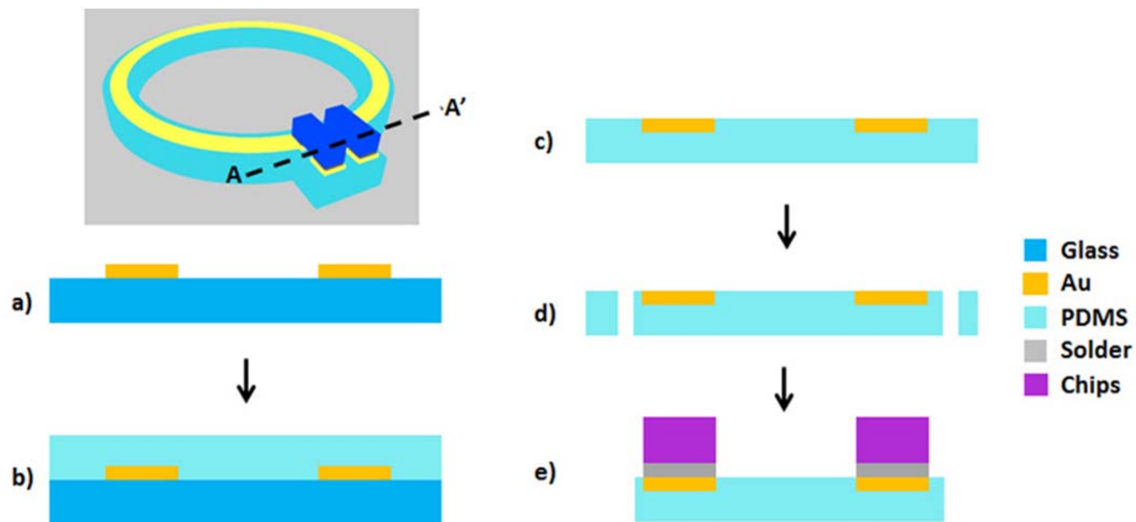

Figure 2.3: Fabrication steps for the metal-on-elastomer. Cross-sectional view along A-A' is illustrated. a) Metal patterning on glass substrate by lift-off, b) PDMS spin-coating and curing, c) Metal transfer after peeling PDMS from glass, d) Laser cutting for the ring shape, e) Solder dip-coating and chip assembly.

2.3.1.1 Metal Layer Deposition via Handling Wafer

In this method, the metal pattern is first deposited and patterned on a handling glass wafer and then transferred to a spun-on elastomer upon peeling [42, 43]. As depicted in Figure 2.3, the fabrication starts with metal lift-off on a glass substrate. A Cr seed layer is not used in the Au evaporation in order to avoid strong metal adhesion to the handling wafer. A 50 nm / 20 nm / 50 nm Au/Cr/Au metal layer is deposited. The Cr layer in the middle serves as a barrier in the soldering process since Au diffuses into the solder rapidly. After the antenna and the electrical interconnects are patterned, a 150 µm-thick PDMS layer is spin-coated on the glass substrate, degassed and cured at 70°C for 30 min. The Au/Cr/Au layer is transferred to the elastomer layer upon peeling the PDMS from the glass substrate. Au is known for its poor adhesion and it adheres to PDMS better than glass or Si. PDMS, with metal on top, is cut into ring shapes using a CO_2

laser in order to be enclosed in the PEU ring. In the preliminary tests, chips are replaced with surface-mount technology (SMT) resistors (metric 2012) and LEDs (metric 1608) for testing. Resistors and LEDs are dip-coated with a low-melting point solder and placed onto the connection pads manually.

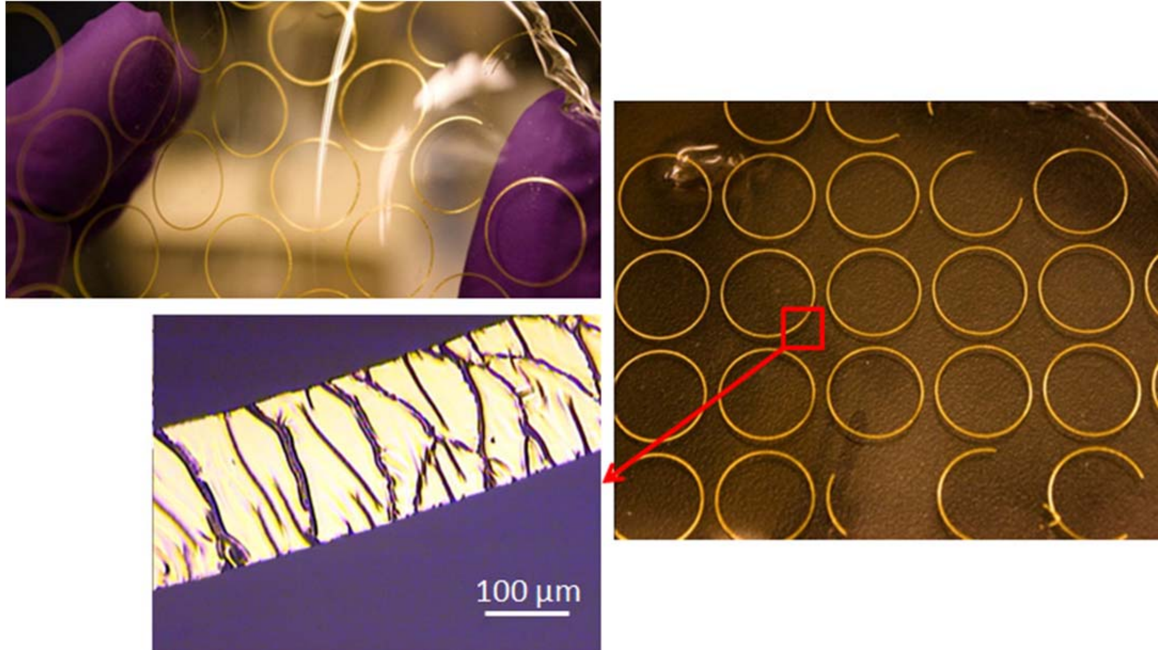

Figure 2.4: Circular metal pattern on PDMS after transfer. Close-up view shows irregular waves on the metal surface profile.

This fabrication method is first tested with a circular metal pattern. Results are presented in Figure 2.4. A wavy metal surface profile is observed after metal transfer due to buckling in the metal. This surface profile is further studied as shown in Figure 2.5. The wave pattern is not periodic but has some repetition. Its amplitude is also irregular and can be as high as 2 µm. It is also observed that buckling is orthogonal to the sides of the pattern. So, its orientation can be controlled by changing pattern aspect ratio as seen in Figure 2.6c. The wavy structure of the metal is due to the linear thermal expansion coefficient mismatch between Au and PDMS [44, 45]. PDMS exhibits a linear thermal expansion roughly 22 times of Au ($\alpha_{PDMS} = 310 \times 10^{-6}$ °C^{-1}, $\alpha_{Au} = 14 \times 10^{-6}$ °C^{-1}) [46]. Buckling of a metal pattern on a PDMS substrate is studied using a simple model by Bowden et al. [44]. The metal layer is directly deposited on the PDMS substrate in that study. However, the thermal process steps are similar; strips of metal adhere to the PDMS substrate at an elevated temperature and the composite structure is subsequently cooled to room

temperature. Equi-biaxial compressive stress experienced by the thin metal layer at temperature T can be calculated using equation (2.1) [44]. Buckling starts when the compressive stress becomes larger than the critical stress defined by equation (2.2).

$$\sigma_o = \frac{E_{Au}(\alpha_{PDMS} - \alpha_{Au})(T_D - T)}{(1 - \upsilon_{Au})} \tag{2.1}$$

$$\sigma_{critical} \approx 0.52\left(\frac{E_{Au}}{1 - \upsilon_{Au}{}^2}\right)^{1/3}\left(\frac{E_{PDMS}}{1 - \upsilon_{PDMS}{}^2}\right)^{2/3} \tag{2.2}$$

$$L \approx 4.36 t_{Au}\left(\frac{E_{Au}(1 - \upsilon_{PDMS}{}^2)}{E_{PDMS}(1 - \upsilon_{Au}{}^2)}\right)^{1/3} \tag{2.3}$$

σ_o: equi-biaxial compressive stress

$\sigma_{critical}$: critical stress for buckling

E_{Au}: Young’s modulus for Au

E_{PDMS}: Young’s modulus for PDMS

α_{Au}: linear thermal expansion coefficient for Au

α_{PDMS}: linear thermal expansion coefficient for PDMS

υ_{Au}: Poisson's ratio for Au

υ_{PDMS}: Poisson's ratio for PDMS

T_D: metal deposition temperature

L: wavelength of the sinusoidal wave pattern

t_{Au}: thickness of the Au layer

The wavelength of the sinusoidal wave pattern is calculated as 8 µm using equation (2.3) from the model. It is measured roughly as 15 µm in Figure 2.5. The difference between theoretical and measured values may be due to the simplification in the model. The model also assumes that both layers are stress-free and perfectly flat before the cooling process.

PDMS, cured at 70°C, shrinks after peeling at room temperature and causes buckling of the metal structure as presented in Figure 2.6. The wavy structure can be used for increasing structural flexibility. It will behave like a serpentine-shaped spring when stretched instead of breaking easily [35, 36]. The effect of the cooling process on the bucking is also studied as shown in Figure 2.7. Two metal transfer processes are performed using different cooling processes while

the glass-metal-PDMS stack is intact. The first process is performed with rapid heating and cooling between 25 °C and 70 °C with an elastomer curing time of 30 minutes. The second process employs a gradual temperature change model where heating and cooling times are 1 hour. Both elastomer layers are peeled off from glass after that. Smoother metal patterns are obtained in the second process compared to the first one. Thermal stress is decreased in the second method due to gradual curing happening in the elastomer. Increase in time enables reflow of uncured elastomer lowering the thermal stress and buckling.

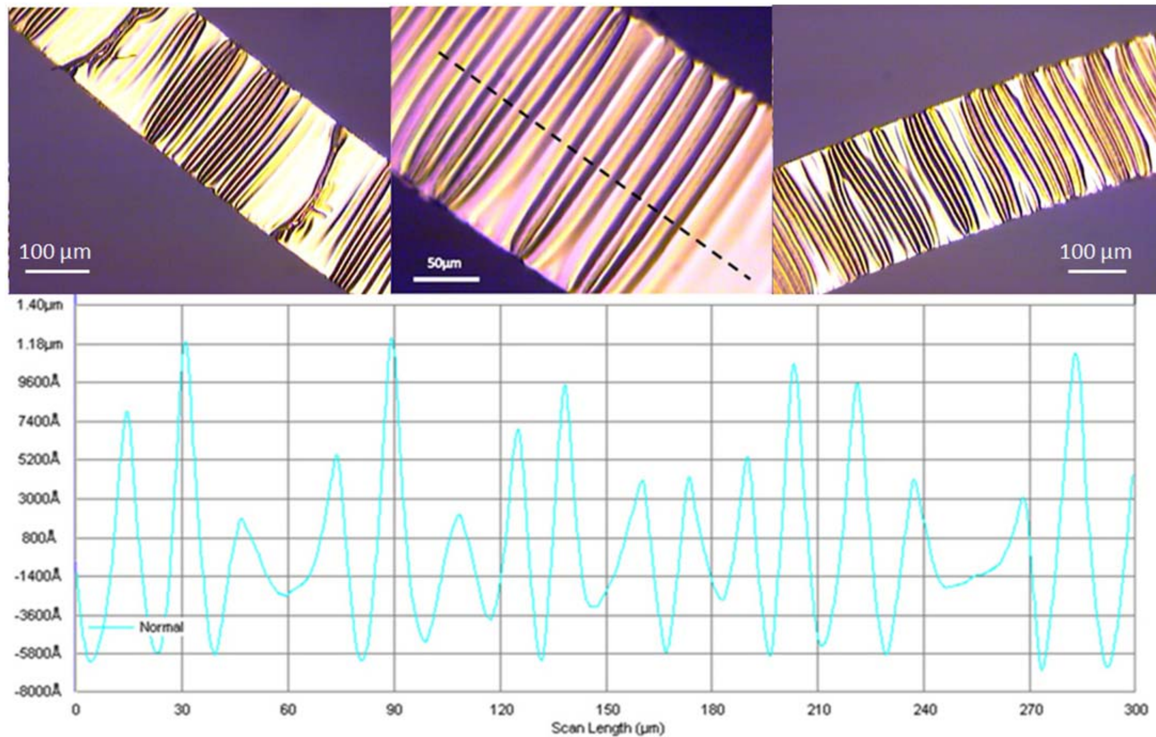

Figure 2.5: Wavy metal structure due to the thermal expansion coefficient mismatch. Surface profile of the metal along the dotted line is plotted. The amplitude of the wave has an irregular characteristic. The peak-to-peak amplitude of the wave can reach up to 2 µm.

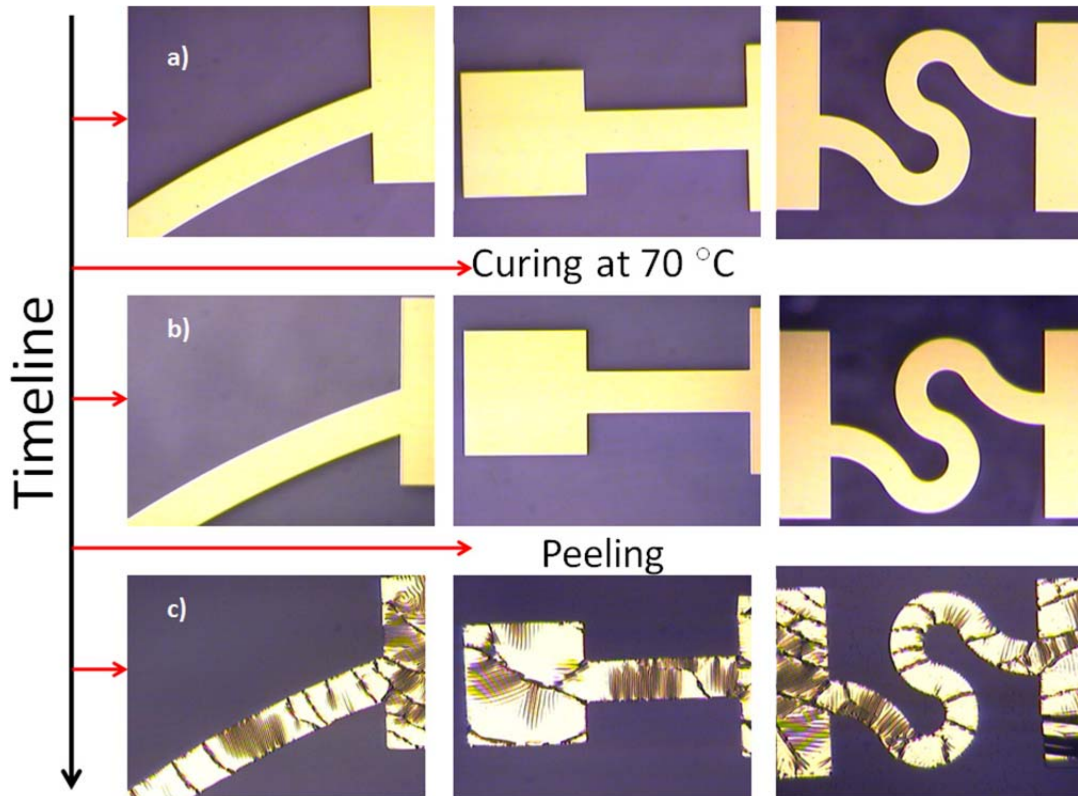

Figure 2.6: Metal-on-elastomer patterns are observed during the fabrication process for buckling. No visible change is observed in steps a) and b). Buckling is presented after peeling at room temperature in step c).

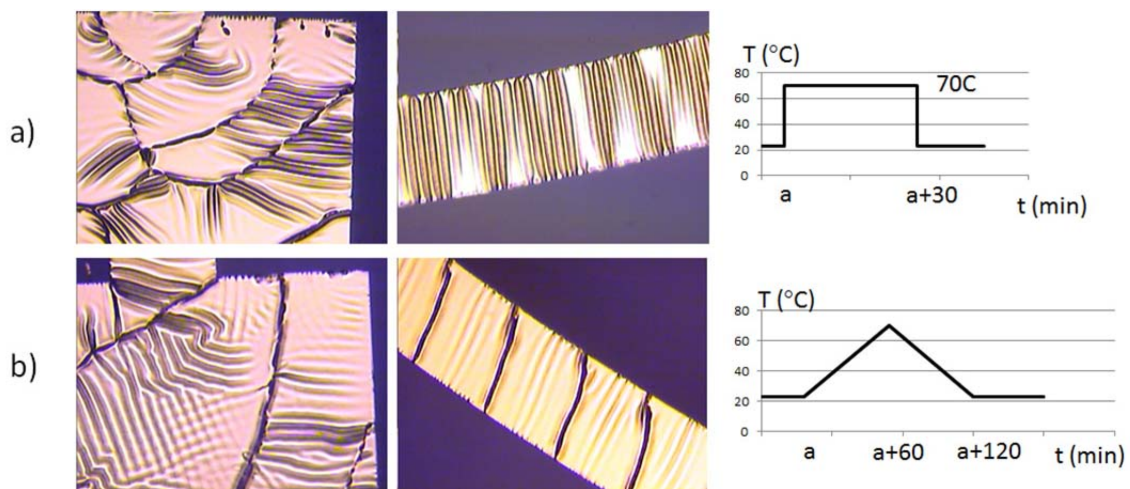

Figure 2.7: Effect of cooling process on buckling: a) Substrate is heated and cooled rapidly. Buckling is more vigorous. b) Heating and cooling is performed gradually resulting in smoothed waves.

Table 2.2 compares theoretical and measured resistance values of the antenna and interconnections from different batches. The resistance of the antenna rises by a factor of 4 after transfer to PDMS. The resistance of interconnections triples. The increase in the resistance might be related to the micro cracks occurring during the transfer. Figure 2.8 shows the assembled SMT resistor and LED with the antenna on the PDMS ring. Conductivity of the metal pattern is also shown with an illuminated LED.

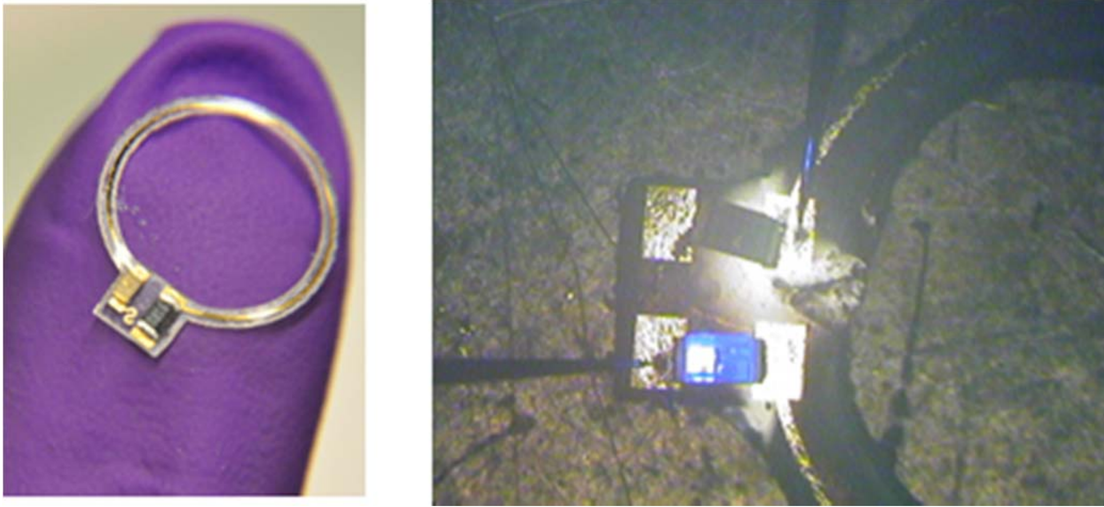

Figure 2.8: Left: Assembled device (actual chips replaced with SMT devices with dimensions similar to the chips for testing the packaging method). Right: Illuminated LED showing the conductivity of the metal pattern.

Ring-shaped metal structures are fabricated on PDMS using the metal-on-elastomer approach and SMT components, representing chips, are assembled. Their conductivity is tested with resistance measurements. However, two drawbacks of the method are low yield and high resistance. Metal layers on the PDMS tend to break easily even during the transfer step. Fractures and cracks can occur during that step. Another factor affecting the yield is the temporary adhesion of the metal to the glass wafer. The metal layer can be washed away during the lift-off since Au adhesion to glass is not strong enough. The resistance values can be improved by increased metal thickness using electroplating. However, submerging semi-adhered Au into a liquid can cause more delamination.

Table 2.2: Comparison of theoretical and experimental electrical conductivity among different batches, before and after transfer to PDMS.

Antenna Resistance (Ω)		Interconnection Resistance (Ω)		
			Type-1	**Type-2**
Theoretical	38.6	Theoretical	1.07	1.03
Before transfer	43.2	Before transfer	17.5	16
Batch-1 after transfer	131.3	Batch-1 after transfer	35.6	38.2
Batch-2 after transfer	178.6	Batch-2 after transfer	52.3	45.6

2.3.1.2 Metal Layer Deposition through Shadow Mask

A metal layer is evaporated onto the PDMS substrate through a shadow mask in order to eliminate the resistance increase during the PDMS peeling step. The shadow mask is fabricated from a 400 µm thick Si wafer using through-etch in a deep reactive ion etcher. A 150 µm thick PDMS layer is spin-coated on a Si substrate and cured as described in the previous chapter. The shadow mask is brought into contact with the PDMS and a 20/100 nm thick Cr/Au layer is evaporated onto this stack as in Figure 2.9. Later, the shadow mask is removed leaving the patterned Cr/Au layer.

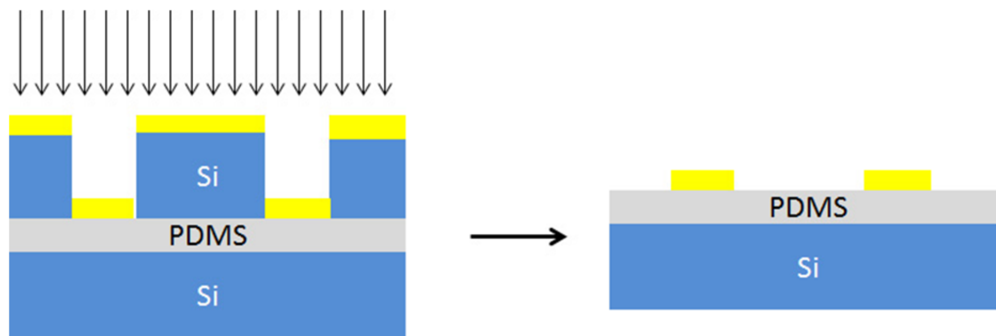

Figure 2.9: The Cr/Au layer is evaporated on PDMS through a Si shadow mask.

Cr/Au-on-PDMS structures made with shadow masking are shown in Figure 2.10. There is less buckling effect compared to the previous fabrication method. A shadowing effect is present at pattern edges where there is less metal deposition. The wafer dome in the evaporator moves wafers along a spherical surface during the evaporation. Metal is deposited onto those regions in

certain wafer positions. They are shadowed by the mask otherwise.

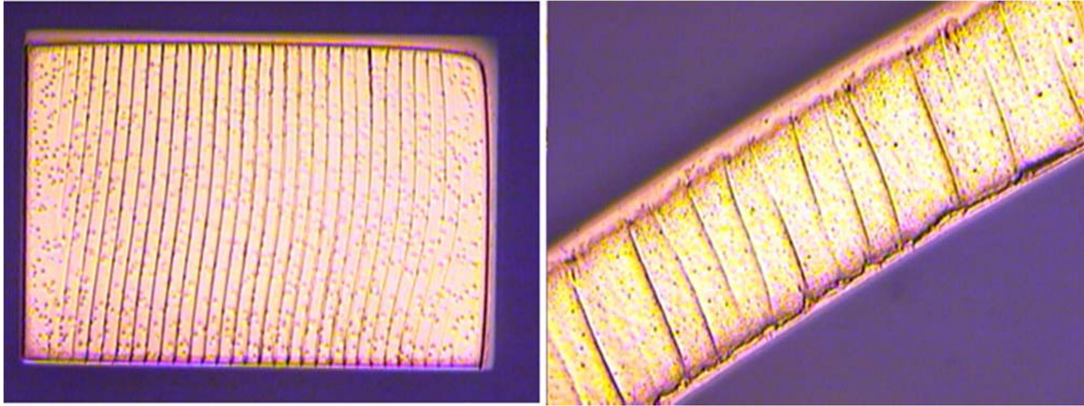

Figure 2.10: Metal-on-PDMS structures made with shadow masking. The metal surface is much smoother compared to the previous fabrication method.

The resistance of the circular metal pattern is measured between 65 and 80 Ω, compared to a calculated resistance of 38 Ω. Deviation from the theoretical resistance value is lower than the deviation in the previous fabrication method.

2.3.2 Solder-Filled Microchannel

This method employs surface treated microchannels as a mold for the metal structure. The metal is formed by filling microchannels with an appropriate alloy. Thus, thick metal structures can be fabricated without electroplating. Alloys are chosen among the ones with indium content in order to increase the wettability of the treated PDMS surface. The melting point is another important aspect for choosing the alloy in order to prevent exposing chips to high temperatures. 51% In 32.5% Bi 16.5% Sn low-temperature solder (Indium Corp.) is chosen for its melting point of 60°C. There are other commercially available solders with lower melting point, as seen in Table 2.3. However, they contain Hg or Pb which are classified as toxic.

The fabrication process is depicted in Figure 2.11. It starts with building a microchannel. For that, an SU-8 mold is built on a Si wafer using conventional photolithography. The ring-shaped SU-8 structure has a mean radius of 5.75 m, a width of 200 µm and a height of 35 µm. This mold is surface-treated with tri-decafluoro-1,1,2,2-tetrahydrooctyl-1-trichlorosilane under vacuum for at least 30 minutes, before 10:1 PDMS mixture is spin-coated on it. Later, it is left in vacuum for degassing and cured at 70°C for 30 minutes. The same procedure is repeated on a bare Si wafer in order to form the bottom layer of the PDMS microchannel. Upon curing, both layers are separated

from Si wafers. Holes are punched onto the first PDMS sheet in order to have access to the microchannel using a Harris Micro-Punch™ (Ted Pella Inc.). Both PDMS layers are exposed to O_2 plasma at 185 mbar and 20 W for one minute. A permanent bond is formed between them when they are brought into contact due to Si-O-Si covalent bonding. Within 10 minutes of the plasma treatment, a droplet of 3-mercaptopropyltrimethoxysilane (MPTMS) solution (0.1M solution prepared in acetonitrile) is delivered to the channel. Upon reaction between the surface treatment agent and hydroxylated PDMS surface, thiol groups are present on the surface making it wettable by liquid solder. Microchannels are left for drying at the room temperature afterwards.

Table 2.3: Commercially available low temperature solders (data from Indium Corp.)

Liquidus Temp. (^{0}C)	**Solidus Temp. (^{0}C)**	**Elemental Composition (% by Mass)**
43	38	42.9Bi 21.7Pb 18.3In 8.0Sn 5.1Cd 4.0Hg
47	47	44.7Bi 22.6Pb 19.1In 8.3Sn 5.3Cd
52	47	44.7Bi 22.6Pb 16.1In 11.3Sn 5.3Cd
56	54	49.1Bi 20.9In 17.9Pb 11.6Sn 0.5Cd
58	58	49.0Bi 21.0In 18.0Pb 12.0Sn
60	60	51.0In 32.5Bi 16.5Sn
62	62	61.7In 30.8Bi 7.5Cd
65	57	47.5Bi 25.4Pb 12.6Sn 9.5Cd 5.0In

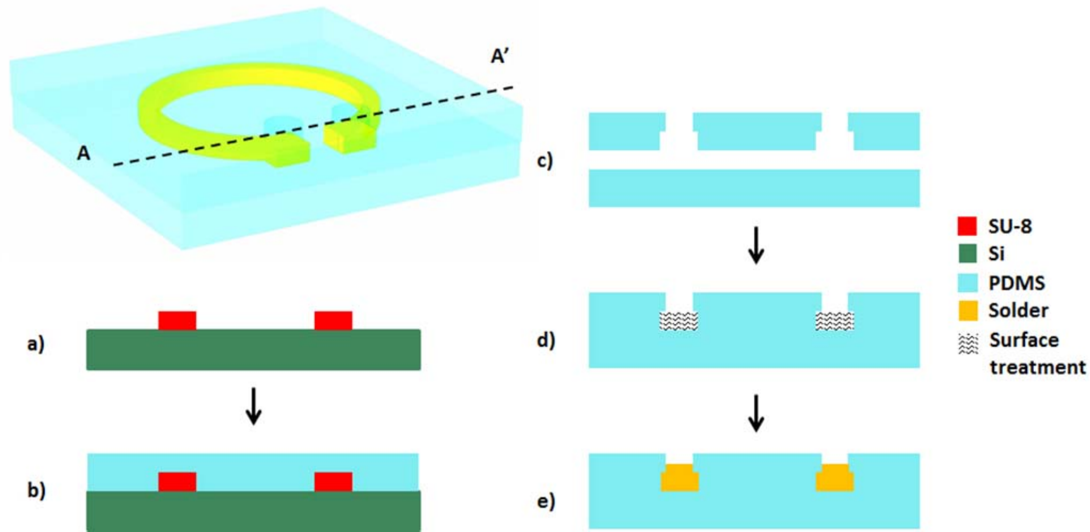

Figure 2.11: Fabrication process for a ring antenna. Cross-section along the connection pads, A-A', is illustrated. a) SU-8 mold on Si wafer for PDMS shaping. b) PDMS is spin-coated on the mold and polymerized. c) The microchannel is formed by PDMS-to-PDMS bonding via O_2 plasma. d) The channel is filled with MPTMS solution, within 10 minutes of the plasma treatment, in order to increase wettability by solder, and left for drying. e) Sample is heated to 75 ℃ and a drop of solder (51% In 32.5% Bi 16.5% Sn alloy) is delivered to the inlet.

Dry channels are placed on a hot plate set at 75°C and heated for 5 minutes in order to heat the channel above the solder melting point. A droplet of liquid solder is delivered to the inlet of the heated channel and a negative pressure is applied to the other inlet in order to drive solder into the channel. House vacuum is used as the negative pressure source and introduced gradually via a valve. After the microchannel is filled with the liquid solder, the sample is cooled to the room temperature. It can be cut into the desired shape using a CO_2 laser.

After the fabrication is completed, rings are first investigated under the microscope. As seen in Figure 2.12, the antenna surface is a rough metallic surface through the transparent PDMS structure. The roughness is most likely due to the cooling process of the solder. This roughness disappears when it is heated above the melting point of the solder. There are bubbles or gaps observed in some of the channels as in Figure 2.13. Those may result in reduced conductance or even disconnected metal structures. Surface-treatment agent or air trapped in the channel is the reason for this failure. Cavities due to trapped surface-treatment agent can occur if the channel is not completely dry during solder delivery. They are avoided by keeping the channels at 75°C for at least 15 minutes to evaporate the solvent before solder delivery. Air trapping occurs depending on the solder delivery speed. It is more common at a solder delivery speed of 6.62 cm/s (circular

channel filled in 5 sec) compared to 0.94 cm/s (circular channel filled in 35 sec).

In addition to those, any defect in the PDMS also translates into a defect in the metal layer as seen in Figure 2.13c. Electrical resistance measurements are also performed on the samples to ensure the connection. Resistances vary between 2.7 and 3.1 Ω depending on the existence of any defects. The measured values are below the 5 Ω limit required for efficient RF power reception.

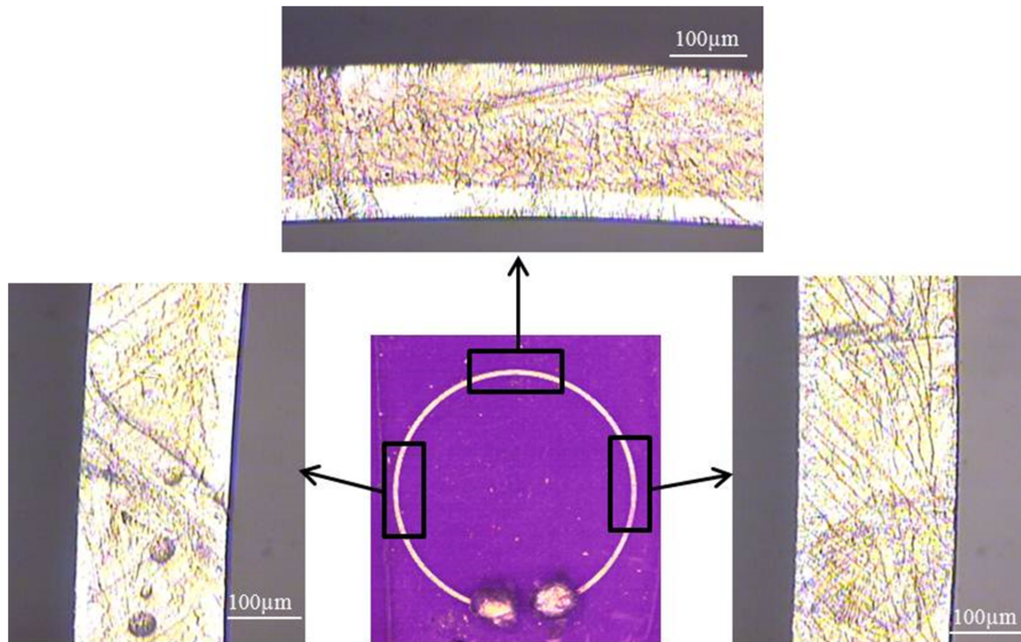

Figure 2.12: Microscope view of the ring antenna from three different regions.

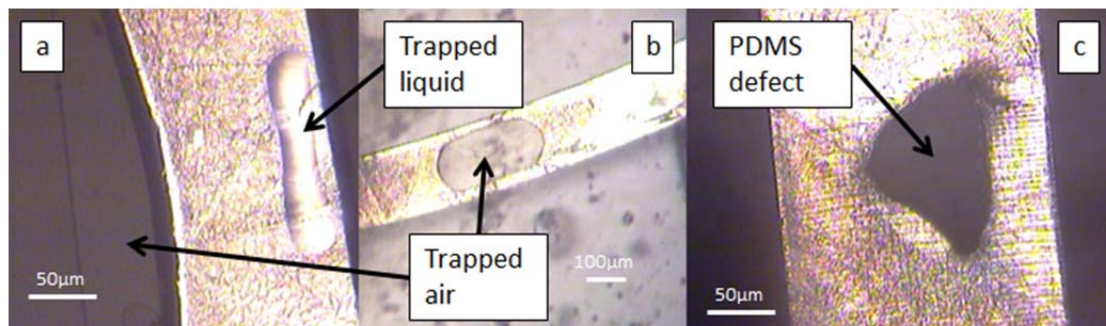

Figure 2.13: Defects observed in the solder-filled microchannels. a, b) Trapped air or surface treatment agent in the microchannel causes a gap or cavity in the metal. c) Top surface of the channel collapsed during PDMS bonding. This resulted in a defect in the metal.

Using a low-temperature solder also provides heat-assisted repairing capability for broken metal structures as demonstrated in Figure 2.14. A solder-filled ring-shaped microchannel is first bent by almost 180^0 in order to cause a break in the metal pattern. Then, the broken antenna is placed onto a hotplate, which is heated to 75 °C. The repair of the broken pattern is observed as the metal melts and fills the hiatus. If repair does not occur immediately, the break region is gently pressed with the tip of tweezers in order to apply pressure. It ensures the repair in case there is a deformation in the microchannel separating two metal pieces. The effect of the deformation can also be seen in Figure 2.14c. This shows another advantage of solder-filled channels over traditional metal processing methods. Using an alloy with a relatively low melting temperature enables in situ repair of fractures.

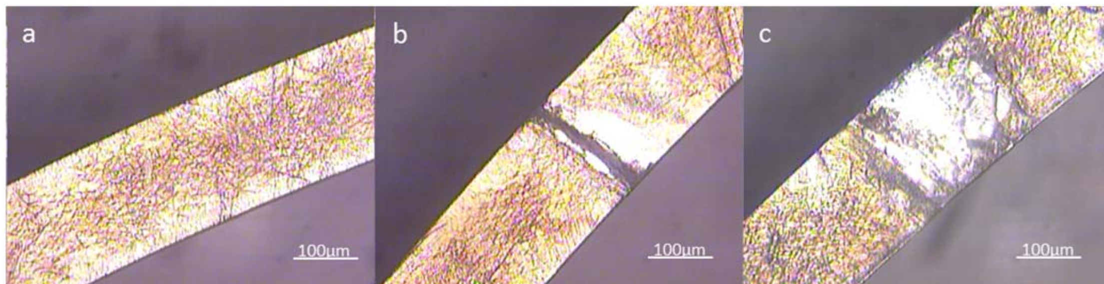

Figure 2.14: Heat-assisted repair of a break in the antenna: a) metal pattern embedded in PDMS before breaking; b) broken metal pattern; c) repaired metal pattern.

2.3.3 Comparison of Fabrication Methods

Low-resistance antenna structures can be fabricated in a simple process with the solder-filled-microchannel method compared to the metal-on-elastomer method. The thickness of the metal is determined by the channel height, which can be two orders of magnitude larger than the thin film thickness. Metal electroplating must be used to achieve a similar metal thickness in the metal-on-elastomer process. Both methods can be considered as simple microfabrication techniques. But the solder-filled microchannel produces an antenna already embedded in a protective PDMS layer while the metal layer in the first method is uncovered. Moreover, defects or cracks can be repaired in the solder-filled-microchannel. This method is more advantageous for building an IOP monitoring device considering all factors.

2.4 Integration Scheme

Preparation of the PDMS package and the molding process is explained in detail in the antenna fabrication. Incorporation of the chip integration process is the focus here. Figure 2.15 shows a

detailed view of the device before it is encapsulated in the tension ring. The yellow structure in the illustration is the metal alloy so the mold will have the same geometrical structure. Yellow squares sticking out of the metal pattern correspond to inlets of the microchannels. Once microchannels are filled with the solder and the metal structure is formed, inlets can be removed. The figure illustrates three chips for the RF circuit, a pressure sensor and an SMT capacitor, which is needed for circuit operation. There will be three interconnections in addition to the antenna. Thus, four microchannels will be used. The mold in Figure 2.16 can be used to form the microchannel network. In Figure 2.16, it is seen that chips are immobilized on the mold by using SU-8 pillars and the connection pads on the chips are aligned to the microchannels, which will be the metal layer after solder-filling. So, the antenna can be connected to a circuit or electronic components at the time of the fabrication. This eliminates the need of wire-bonding, which may cause fracture under stress. A typical Si mold can be fabricated through a series of photolithography and deep reactive ion etching processes.

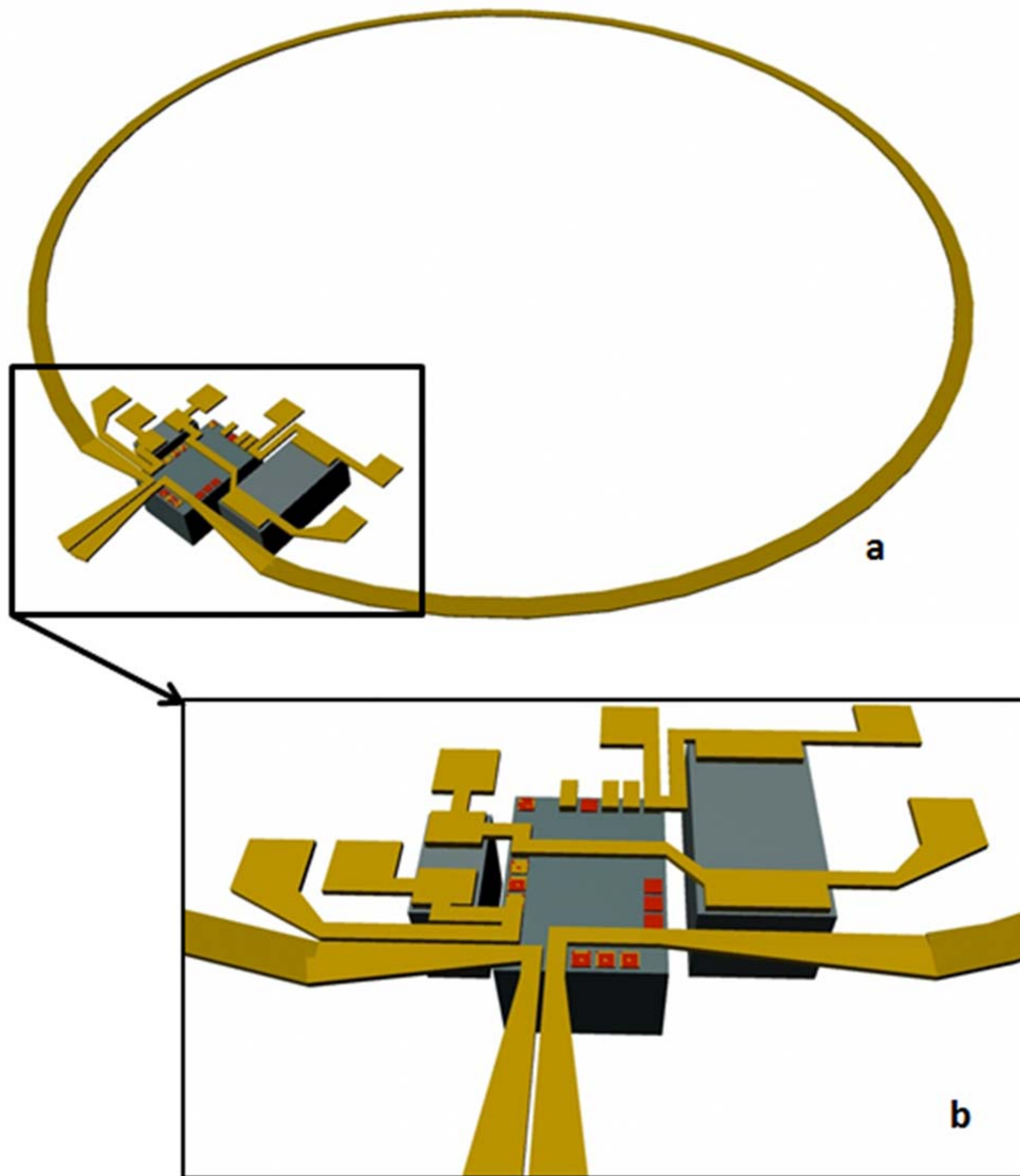

Figure 2.15: Illustration of the device without the PDMS structure and the tension ring. a) The general view including the ring antenna and the chips. b) The close-up view of three interconnections. Each of them requires two inlets for the fabrication.

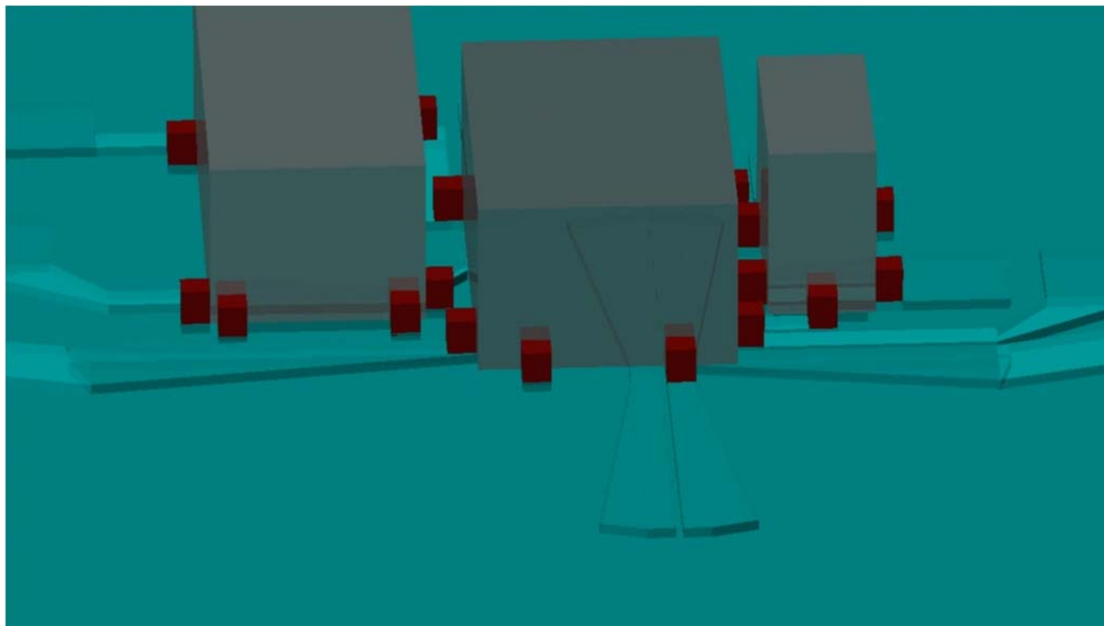

Figure 2.16: The mold, made of Si, for the PDMS structure and the chips to be integrated. Red pillars represent SU-8 structures for immobilizing the chips.

2.5 Compatibility with PEU Ring

Metal carrying PDMS rings from both metal-on-elastomer and solder-filled microchannel processes are tested for their compatibility with the PEU ring fabrication method and their effect on the water-induced shape memory characteristic of the polymer ring. Polymer compositions were developed based on cross-linked polyetherurethanes (PEUs) synthesized at the University of Washington Engineered Biomaterials Laboratory, Bioengineering Department, University of Washington (Seattle, WA). PEU coating and testing were completed with the help of Felix Simonovsky.

In order to make PEU ring samples with embedded metal/PDMS structure, PDMS rings are placed into the plastic mold consisting of two circular cavities. Then, these two parts are screwed with bolts and a liquid composition is injected into the mold. After that the mold is placed into the oven for several hours at about 80ºC to complete polymerization. When the reaction is finished a mold with completely monolithic PEU rings with embedded PDMS part is unscrewed, opened, and obtained rings can be removed.

The effect of embedded metal/PDMS structure on the water-driven shape memory property of the PEU ring is tested. Time required for a dehydrated squeezed ring to relax to its circular shape when submerged into water is called resilience time. If the PEU ring is to be used as a capsular tension ring, shorter resilience time is required for precise implantation. As it becomes longer, the

risk of implant dislocation becomes higher. Resilience time is recorded for PEU rings with and without embedded PDMS structure. Squeezed rings are dehydrated at 80 ºC overnight to keep their shape. Resilience time is measured as few seconds for PEU rings without PDMS structure. It increases to 24 seconds for the PDMS/PEU composite. The increase in resilience time can be explained by the difference in water intake capability due to the volume replaced with PDMS. It can be improved with tailoring polymer composition.

2.6 Conclusion

The design of a flexible packaging method for the IOP sensor is presented along with the results from the antenna fabrication. The presented method achieves the antenna fabrication and the chip integration at one step. The solder-filled-microchannel approach is promising for fabrication of the desired IOP sensor as well as other flexible structures. It allows fabrication of thick metal layers in a simple fabrication scheme. It also offers the capability of repairing breaks, which may occur after the fabrication. However, its application is limited to alloys with low melting point and better wetting characteristics for the PDMS surface.

CHAPTER 3. PROTOTYPE OF THE INTRAOCULAR PRESSURE MONITORING DEVICE

3.1 Introduction

In Chapter 2, a novel packaging and antenna fabrication method was introduced for an IOP monitoring device. This is achieved using solder-filled microchannels to fabricate metal structures embedded in a flexible and biocompatible substrate. In this chapter, a device prototype assembled using the aforementioned method is presented.

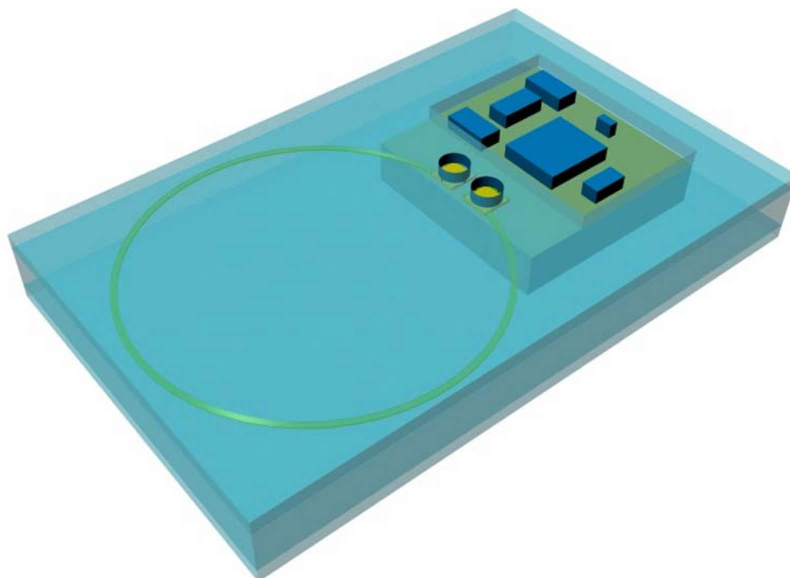

Figure 3.1: Illustration of the prototype device. Chip, sensor and circuit components are first assembled on a PCB, and then embedded in PDMS for antenna fabrication.

3.2 Device Prototype

The IOP monitoring device contains three main components: the antenna for power/data transmission, the RF chip for power harvesting and pressure-to-frequency conversion, and the pressure sensor for physical measurement. However, surface-mount circuit elements are also required for RF chip operation in its first generation. Additionally, connection pads are needed for on-the-bench calibration and characterization of the first prototype, which increase the size and complexity of the device. It is appropriate to assemble the first prototype on a fiberglass printed circuit board (PCB) since it is not implanted and is used for testing and characterization. The RF chip and surface mounted components are first assembled onto the PCB. Then, it is integrated with the antenna using the solder-filled microchannel method. Since the chip requires no external

components, the PCB can be eliminated in an implantable device and the solder-filled microchannel method can be used for the interconnection between chips.

3.3 Prototype Fabrication

3.3.1 Parts and Part Assembly

A 22 mm × 18 mm PCB is employed in the prototyping phase. It is printed by Sierra Circuits, Inc. (Sunnyvale, CA). As seen in the PCB layout (Figure 3.2), RF chip, pressure sensor, an SMT inductor, three SMT capacitors and three SMT resistors are assembled by AmTECH Microelectronics Inc. (San Jose, CA). SMT components are assembled through wave soldering while the RF chip and the sensor are wire-bonded to the PCB.

The RF chip is provided by Prof. Brian Otis's Wireless Sensing Lab in Electrical Engineering Department, University of Washington, Seattle. It has a low-power circuit, which can be powered wirelessly at radio frequencies [13]. The circuit converts capacitance and temperature into frequency and modulates the backscattering frequency in order to transmit the measurement to an external receiver. It can be configured for single or multiplexed data transmission. An off-the-shelf capacitive MEMS sensor, with a range of 0.5-1.3 bar and an average sensitivity of 0.451 pF/bar, is employed for pressure measurements (E1.3N, microFAB Bremen GmbH, Germany). SMT circuit components are used for impedance matching and voltage regulation. Connection pads are employed for changing circuit configuration, testing harvested power and voltage as seen in Table 3.1.

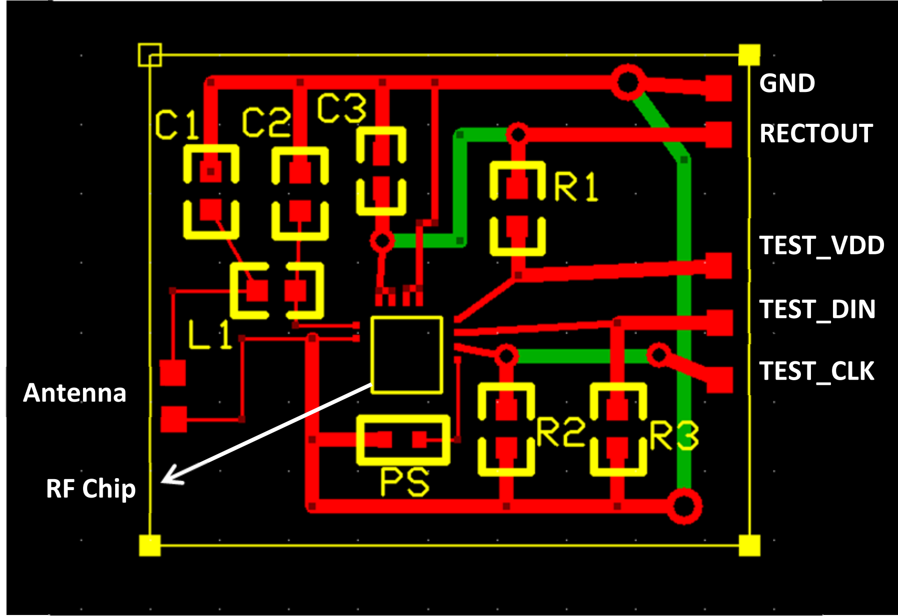

Figure 3.2: PCB layout of the prototype. PS: Pressure sensor; R1,R2, R3: SMT resistors; C1,C2, C3: SMT capacitors; L1: SMT inductor.

Table 3.1: Connection pads on PCB and their function.

Connection Pad	Function
GND	Ground
RECTOUT	Harvested voltage/power
TEST_VDD	Shift register voltage for chip configuration
TEST_DIN	Data input for chip configuration
TEST_CLK	Clock

3.3.2 Antenna Fabrication and Integration

The fabrication process starts with casting two PDMS layers. They are bonded to form a microchannel, which is later filled with solder. An SU-8 mold on Si wafer is employed for the first PDMS layer. The pattern shown in Figure 3.3 is used for the SU-8 mold. The width of the microchannel is increased from 200 µm in the circle to 1 mm in the rectangular part (connection pads) gradually in order to achieve a smooth solder flow. The mold is made with conventional photolithography in a contact mask aligner.

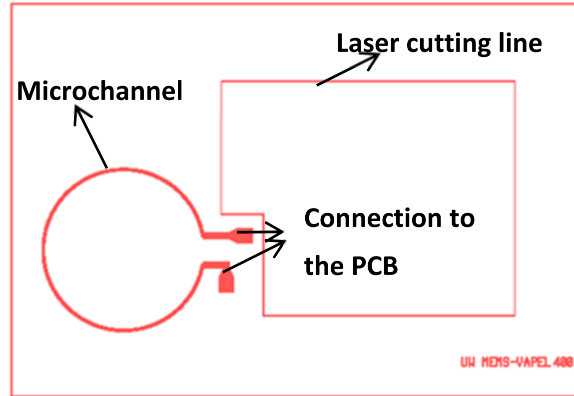

Figure 3.3: The pattern for the SU-8 mold. Thinner lines indicate the laser cutting locations. The inner region of the PDMS is cut out in order to access the PCB.

The complete process is depicted in Figure 3.4. The SU-8 mold is surface-treated with tri-decafluoro-1,1,2,2-tetrahydroctyl-1-trichlorosilane under vacuum for at least 30 minutes. A 10:1 PDMS mixture is spin-coated on the mold. It is left in vacuum for degassing and cured at 70°C for 30 minutes. For the second PDMS substrate, a 10:1 PDMS mixture is poured into a petri-dish and degasses. PCB is submerged into PDMS layer upside-down before curing. Hence, the top surface of PCB has a flat PDMS coating, critical for PDMS-to-PDMS bonding. After curing, both PDMS substrates are peeled off. Inlet holes are punched at the ends of the microchannel pattern. They are bonded upon O_2 plasma treatment. Connection pads on the PCB are aligned to the rectangular parts at the ends of the microchannel pattern in order to achieve antenna-to-PCB connection.

The microchannel surface is treated with MPTMS to increase wettability and left at room temperature to dry. Molten solder is delivered to the microchannel at 75 °C. The temperature inside the microchannel is critical for a continuous solder delivery. Thus, the device is left on a hot plate set to 75 °C for 10 minutes before the delivery. The temperature on the device surface is regularly checked using a thermocouple. A volumetric glass pipette is filled with molten solder prior to the process. A heating tape is wrapped around the pipette in order to keep the solder molten. The tip of the glass pipette is aligned to the inlet of the microchannel right before the delivery. The molten solder moves into the microchannel with the help of gravity most of the time. However, negative pressure is also connected to the other inlet in order to propel the solder into the channel. Once the solder delivery is completed, the device is cooled down to room temperature and the PDMS is cut along the lines shown in Figure 3.3 to get access to the PCB.

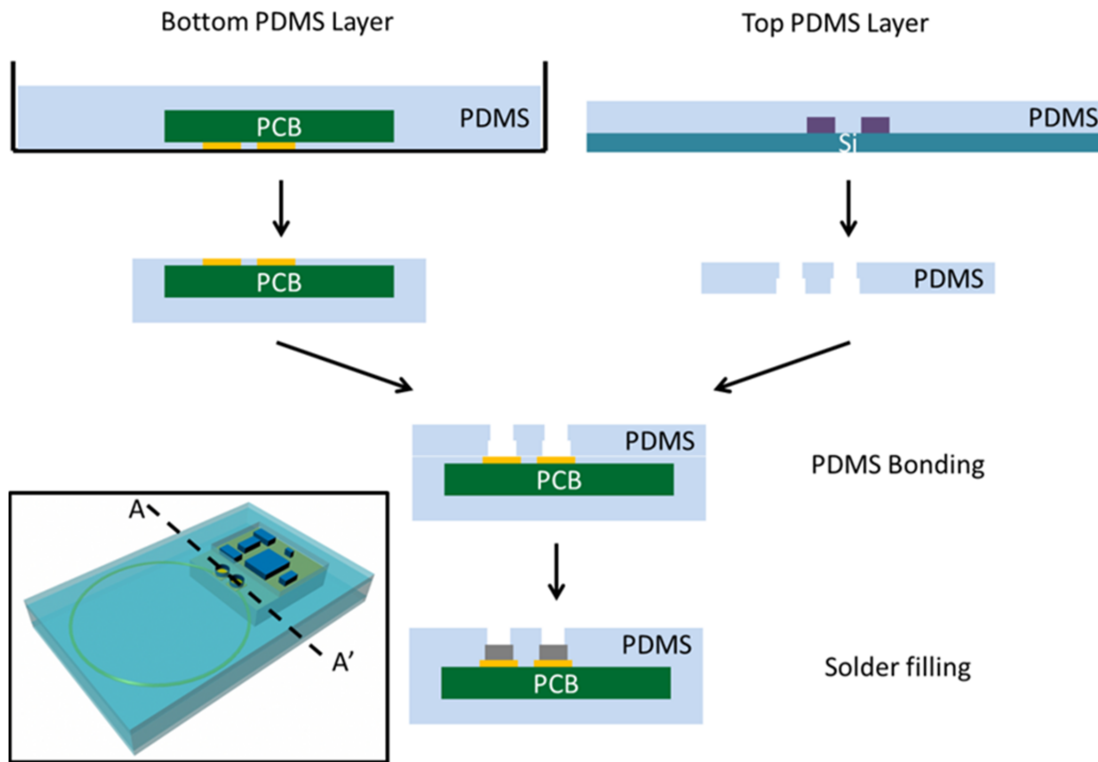

Figure 3.4: Schematic view of the fabrication process for the antenna-PCB integration. Cross-section is along A-A'.

3.3.3 Fabrication Results

An antenna pattern is successfully integrated with an embedded PCB according to the fabrication process explained in detail in the previous section (Figure 3.5). Close-up views of the antenna show a rather rough metal surface, which occurs during the cooling process of the solder. One problem observed during the device fabrication is the weak adhesion between the PCB and the PDMS. This leads to molten solder leaking under the PDMS cover and shorting pads on PCB if the solder is propelled with a large force. However, this is not considered as a major problem since there will not be any PCB used in the final device. Loop antenna resistance is measured as 3.4-3.5 Ω, which is below the 5 Ω limit required for efficient RF power reception.

Two types of PCBs, completely assembled boards and boards with SMT components, are used in the fabrication process. PDMS around the chip and the sensor is left intact in order to protect them if an assembled board is used in the fabrication. For boards with SMT components, chip and sensor wire-bonding is performed posteriorly. Since the highest process temperature is 75ºC, it does not present any risk of thermal damage to the chips or the substrate.

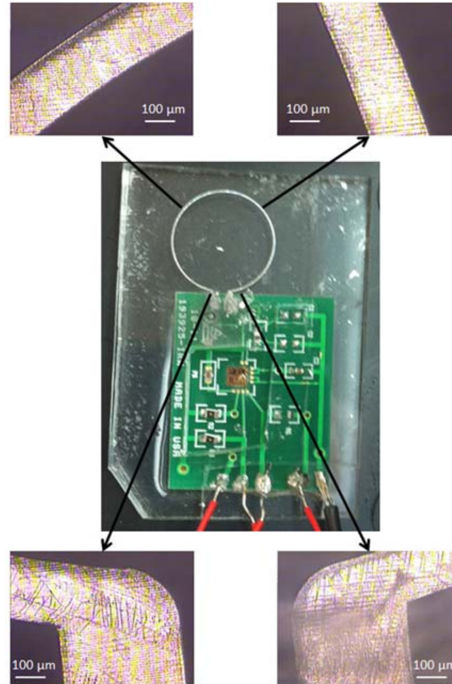

Figure 3.5: Antenna and PCB interconnected and embedded in PDMS. The top surface of PDMS is cut in order to get access to the board. The close-up views show that the ring-shaped metal structure does not have defects.

3.4 Conclusion

The IOP monitoring device prototype is introduced and fabricated. The solder-filled microchannel process is modified for PCB encapsulation and antenna integration. Results show that the PCB is successfully embedded into PDMS and integrated with the antenna. The presented method can be used for biocompatible packaging of microsystems and sensors.

CHAPTER 4. SOLDER-FILLED MICROCHANNEL ANTENNA PERFORMANCE

4.1 Introduction

In Chapter 3, an antenna is integrated to the chip and sensor using the solder-filled microchannel method. That device prototype is encapsulated in a bio-compatible package. In this chapter, the device prototype is powered wirelessly using the integrated antenna. The effect of distance on harvested power and safety limits of RF exposure are analyzed. Lastly, wireless data transmission is presented.

4.2 RF Power Transfer

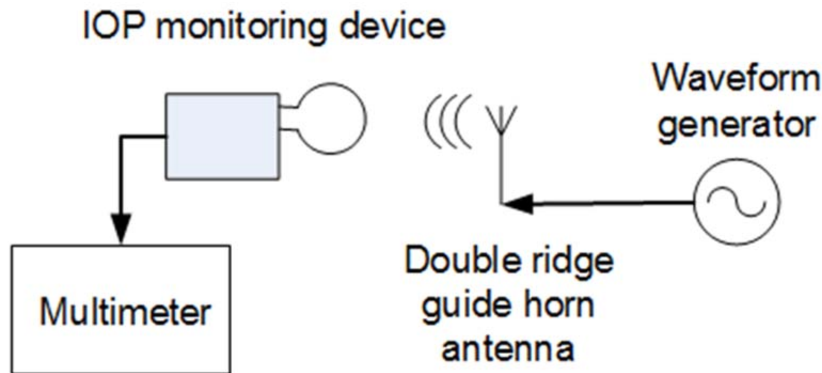

Figure 4.1: Test setup for RF power transfer to the prototype.

The setup illustrated in Figure 4.1 is used to demonstrate functionality of the antenna through the wireless power transfer to the RF chip. A double ridge guide horn antenna is connected to an RF signal generator (E4438C ESG Vector Signal Generator, Agilent Technologies) in order to transmit power to the device. The distance between the antenna and the device is varied as 0, 1 and 2 cm. The device is not touching the antenna due to the large cavity inside the antenna when it is placed at 0 cm. The rectifier output of the chip, which is also the voltage supply, is monitored using a multimeter. Harvested/dissipated power in that node is calculated using measured voltage and current values for each transmitted power level. Equivalent isotropically radiated power (*EIRP*) is calculated as:

$$P_{RF} + G = EIRP \qquad (2.4)$$

P_{RF} is the power supplied by the signal generator; G is the antenna gain and equal to 9 dBi for the horn antenna. Frequency for the most efficient power transfer is determined as 2.716 GHz by frequency sweeping from 0.5 GHz to 6 GHz. This frequency is used for the remainder of the test.

The transmitted power is increased in steps of 1 dBm until the voltage at the rectifier output exceeds 1.5 V. Figure 4.2 shows the harvested power plotted with respect to *EIRP*. It is seen that the harvested power value is above the critical power value of 2.3 μW for the RF chip when *EIRP* is approximately 15.4 dBm and 18.2 dBm form a transmission distance of 1 cm and 2 cm respectively [13]. It should also be noted that no matching network is used in this experiment.

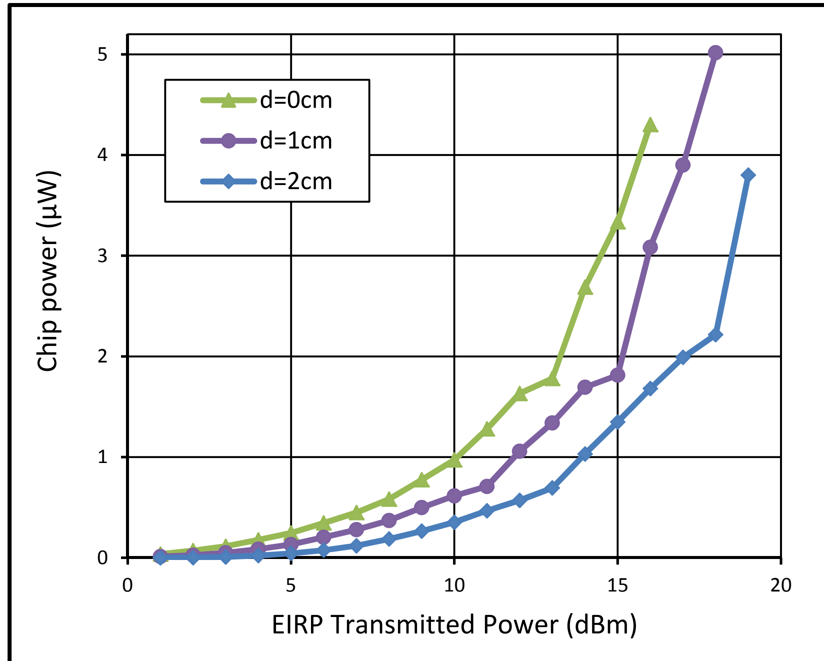

Figure 4.2: Power transferred to the chip at various transmitted power levels and transmission distance.

The amount of power transferred to the chip through an RF transmitter depends on the distance and the materials between the device and the transmitter as well as their alignment. The alignment is usually considered a problem for devices floating within the anterior chamber. However, an IOP monitoring device embedded in a capsular tension ring does not exhibit this problem since the ring is designed as an immobilized implant. The implant location is approximately 5 mm inside from the surface of the cornea. Thus, the presented transmission distance of 1-2 cm can be used in the final device. However, decreased transmission efficiency should be expected for an implanted device due to the 5 mm thick water/tissue slice.

Power transmission can be improved by using a multiple turn loop antenna and a matching network if needed. It is possible to build 2-turn and 3-turn loop antennas within the given space constraints as shown in Figure 4.3. Metal width is kept at 200 μm while edge-to-edge distance

between metal curves is 100µm. In addition, the frequency for the peak power transfer can be adjusted to 2.4 GHz, which is in an unlicensed spectrum.

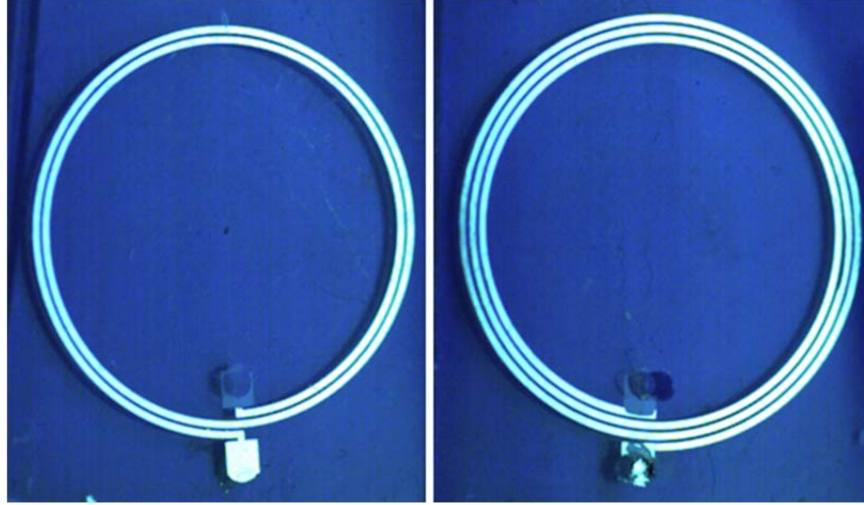

Figure 4.3: 2-turn and 3-turn solder-filled microchannels that can be used as an antenna.

4.3 RF Exposure Limit

An important aspect of a wirelessly powered implanted biomedical device is the level of electromagnetic power applied to the human body. For the IOP monitoring device, the GHz frequency range has the advantage of low tissue absorption. However, high power exposure can lead to a localized temperature increase of 1-2 °C and cause damage in the tissue and thermoregulatory system. The Institute of Electrical and Electronics Engineers (IEEE) has set the maximum permissible exposure (MPE) for the frequency range of 0.3-3 GHz as [47]:

$$MPE\ (W/m^2) = \frac{f(in\ MHz)}{30} \tag{2.5}$$

Thus, MPE for 2.716 GHz is calculated as 9.05 mW/cm^2. Electromagnetic power density of the tissue surface is calculated using:

$$Power\ density\ (mW/cm^2) = \frac{10^{(P/10)}}{4\pi R^2} \tag{2.6}$$

P: transmitted power in dBm

R: distance between antenna and tissue surface in cm

Power density is calculated as 5.63 mW/cm^2 for the transmission distance of 1 cm and 1.82

mW/cm^2 for the transmission distance of 2 cm. The implant is assumed to be 0.3 cm behind the cornea. Both power density values are much lower than MPE and in a range where considered to be safe.

4.4 Transmission of Measurement Results

After RF power transmission is established, the device is tested for transmission of measured capacitance and temperature values. The RF chip used in the device can be operated in 3 modes: (1) reference capacitor transmission mode, (2) pressure transmission mode, and (3) temperature transmission mode. In each mode, the backscattered signal is modulated according to the measurement result. So two frequency components, carrier frequency (f_c) and deviation in frequency due to the measurement result ($\Delta f_R, \Delta f_P, \Delta f_T$), can be observed in its frequency spectrum. The measurement setup illustrated in Figure 4.4 is used for observing the backscattered signal for each mode. The RF signal is transmitted to the device using the RF signal generator (E4438C ESG Vector Signal Generator, Agilent Technologies) and the horn antenna. Backscattered signal is isolated from the transmitted signal using a directional coupler (Krytar, 4080180) and analyzed with a spectrum analyzer (RSA3408A Real-Time Spectrum Analyzer, Tektronix).

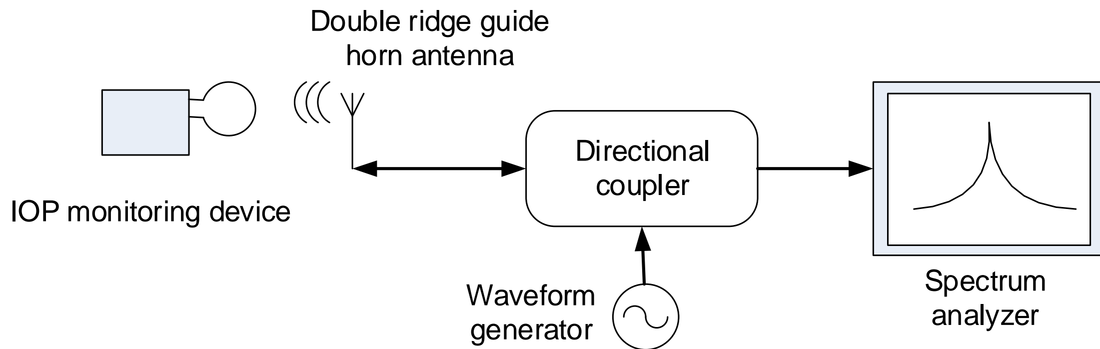

Figure 4.4: Test setup for data transmission from the device.

The frequency spectrum with the backscattered signal (at atmospheric pressure and room temperature) is plotted in Figure 4.5 showing three modes of the RF chip. The side-band for each mode is clearly distinguishable showing that the antenna is performing data transmission as expected. The difference between the carrier frequency and the side-bands is linearly related to the measured parameter.

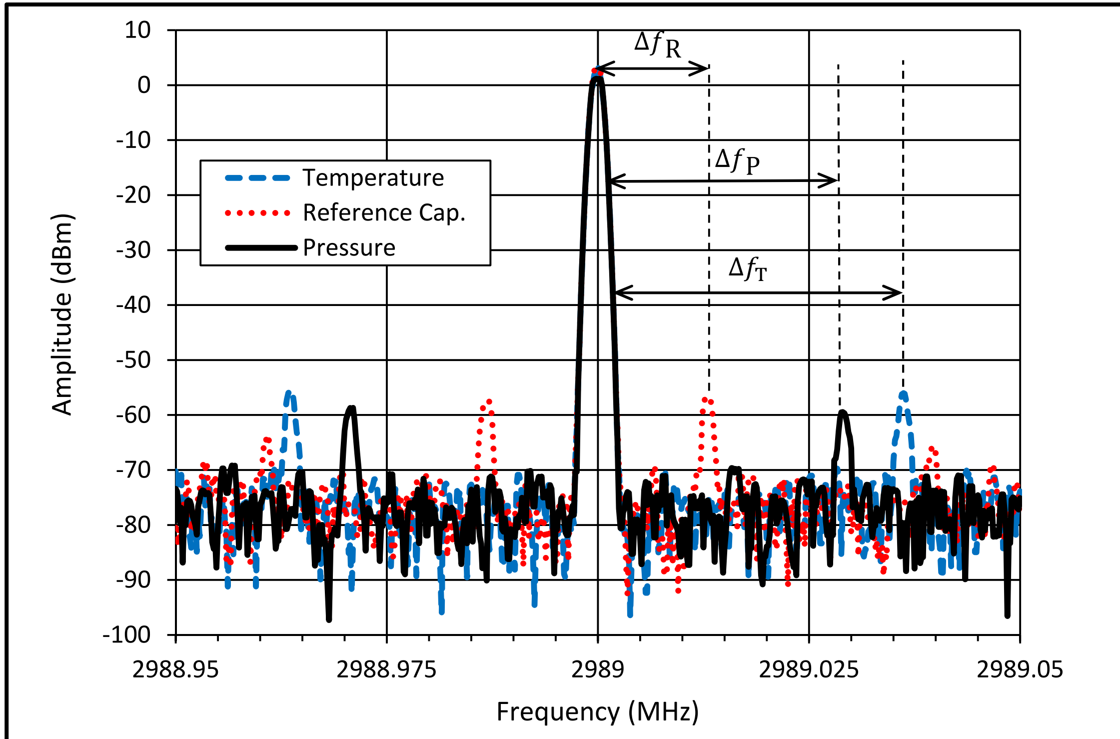

Figure 4.5: Frequency spectrum of the backscattered signal in three measurement modes, at room temperature and atmospheric pressure.

4.5 Conclusion

The solder-filled antenna is tested for transferring data and power to the prototype device. Results show that the device can be powered wirelessly from 2 cm, which is an applicable distance for an outside transceiver. Electromagnetic power density on the tissue surface is lower than the maximum permissible exposure limit for that case. The backscattered signal for the programmed chip mode is successfully received. Each mode is clearly visible in the frequency spectrum of the received signal. The solder-filled antenna in the prototype is functional as expected.

CHAPTER 5. MECHANICAL PROPERTIES OF THE SOLDER-FILLED ANTENNA STRUCTURE

5.1 Introduction

Once the device operation has been established, mechanical endurance of the composite structure is studied. Mechanical properties of PCB-embedded PDMS will be very different from the actual implantable device due to the large size of the PCB. A mockup device is fabricated and used for analyzing mechanical properties of the solder-filled antenna structure.

5.2 Mockup Device

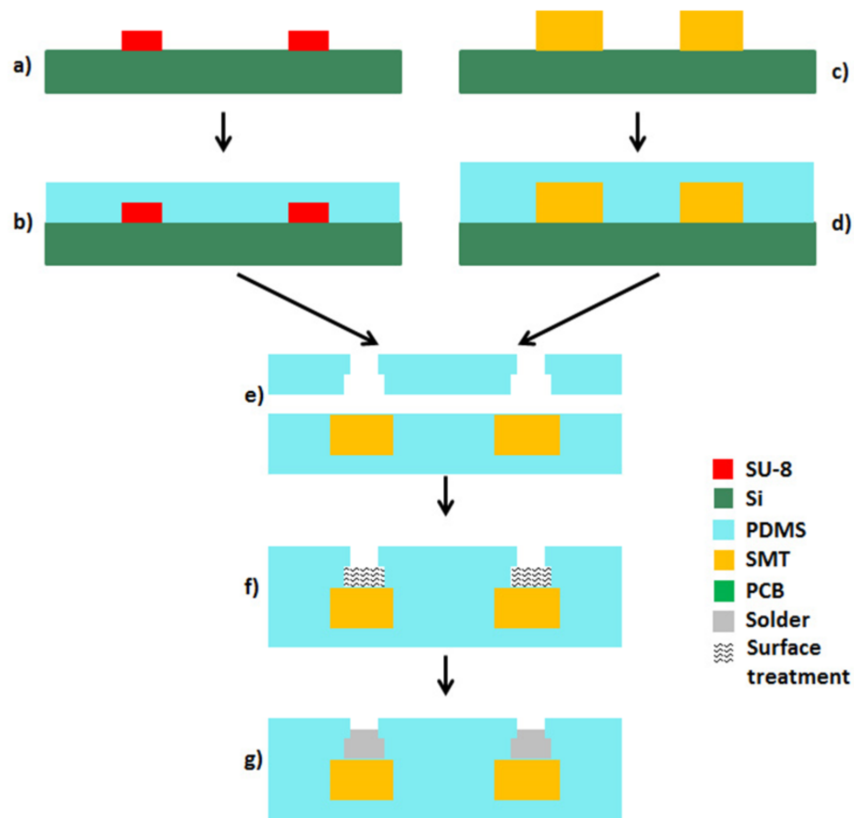

Figure 5.1: Fabrication process for the mockup device. a) SU-8-on-Si mold; b) PDMS spin-coating on the mold; c) SMT components on a Si wafer; d) PDMS coating on SMT components and peeling from the wafer; e) PDMS-to-PDMS bonding upon O_2 plasma treatment; f) surface treatment on the microchannel surface; g) solder delivery.

Chips in the final device are replaced with dummy SMT components similar in size. SMT components are connected through a loop antenna. The fabrication process is illustrated in Figure

5.1. It starts with photolithography for a SU-8-on-Si mold required for microchannel patterning. A 10:1 PDMS mixture is prepared and spin-coated on this mold. It is peeled off the mold after a 30 minute curing step at 60 °C. On a separated wafer, SMT components are immobilized using magnets placed beneath the wafer. They are coated with a 10:1 PDMS mixture and cured at 60°C for 30 minutes. SMT components detach from the wafer upon peeling off the PDMS layer. Two PDMS structures, the one with the antenna pattern and the other with embedded SMT components, are aligned for connecting the antenna pattern to connection pads on SMT components and bonded upon treatment with O_2 plasma. The microchannel surface is treated with MPTMS in order to increase surface wettability. Finally, the channel is filled with solder at 75°C and cooled to room temperature.

5.3 Measurement Setup

The measurement setup is illustrated in Figure 5.2. The mockup device is anchored at the edge of a probe station chuck. A point load is applied on the PDMS using a probe station manipulator. Total resistance of the device is monitored by probing connection pads on the SMT resistors while the PDMS is bent and released. Bending of the PDMS is observed using a camera. Whole bending cycle is recorded and the amount of deflection is measured by pixel counting. Thickness of the PDMS stack is measured beforehand using a micrometer and used as a scale.

Applied force and stress is calculated using the cantilever beam load-deflection equations:

$$d(x) = -\frac{Fa^2}{6EI}(3x - a) \quad \text{for } a \leq x \leq L \tag{5.1}$$

$$\frac{1}{\rho} = -\frac{F}{EI}(a - x) \tag{5.2}$$

$$\epsilon_{max} = \left|\frac{h_{max}}{\rho}\right| \qquad \sigma_{max} = E\epsilon_{max} \tag{5.3}$$

d: cantilever deflection

a: load position with respect to the anchor

ρ: cantilever curvature

h_{max}: maximum distance of the antenna from the neutral axis

L: cantilever length

E: Young's modulus

I: moment of inertia

ϵ_{max}: maximum strain

σ_{max}: maximum stress

The applied force is calculated using the deflection at the tip of the cantilever using equation (5.1). Then, curvature, maximum strain and stress are calculated for $x = 0$, maximum stress point, using equations (5.2) and (5.3). Maximum applied stress and strain values are used to evaluate the antenna endurance.

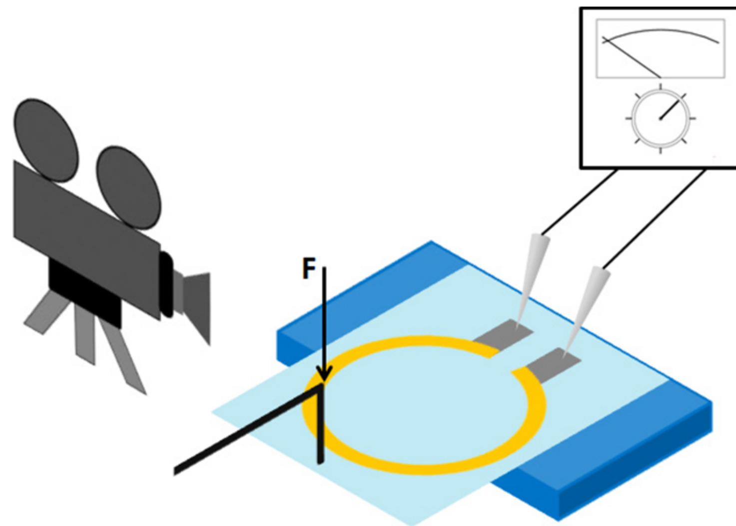

Figure 5.2: Illustration of the test setup. A point load is applied at the edge of the PDMS while bending is observed with a camera and resistance change is observed with a multimeter.

5.4 Results

Testing of a mockup device (Device-1 in Figure 5.4) is shown in Figure 5.3. The antenna resistance is presented in each bending step. It can be seen that the resistance change is below 0.078 Ω (2.83%) until step-4 where a maximum stress of 17 kPa is applied. A larger amount of resistance increase is observed after that step and infinite resistance is observed after step-5. The test is repeated with 5 other devices. The resistance change with the applied stress is plotted until the connection is lost in Figure 5.4. Maximum stress applied on the antenna without disconnecting the metal pattern is 33.4 kPa. The increase in resistance is measured as 0.022 Ω (0.62%) at this stress level. However, a larger resistance increase is observed at lower stress levels in some of the devices. It is also observed that the antenna resistance is restored to its initial value upon release of the load. A second test is employed to investigate the reproducibility of this

observation. The substrate is bent 90° with respect to the initial position applying a maximum stress of 116 kPa and relaxed back to the initial state. The test is repeated 50 times for each of the three samples while monitoring the antenna resistance. The change in the resistance is plotted in Figure 5.5. The histogram of the measured values is also plotted with respect to the initial resistance in Figure 5.6. Both plots show that resistance fluctuates around the initial value. Maximum antenna resistance is observed in the 49th bending cycle as 5.28 Ω. This value is still within reasonable limits for efficient RF power transfer. Arithmetic mean and standard deviation of the antenna resistance ($\frac{R}{R_{initial}}$) is calculated as 0.973 and 0.248, respectively. Maximum deviation is observed as 0.852 in a single case.

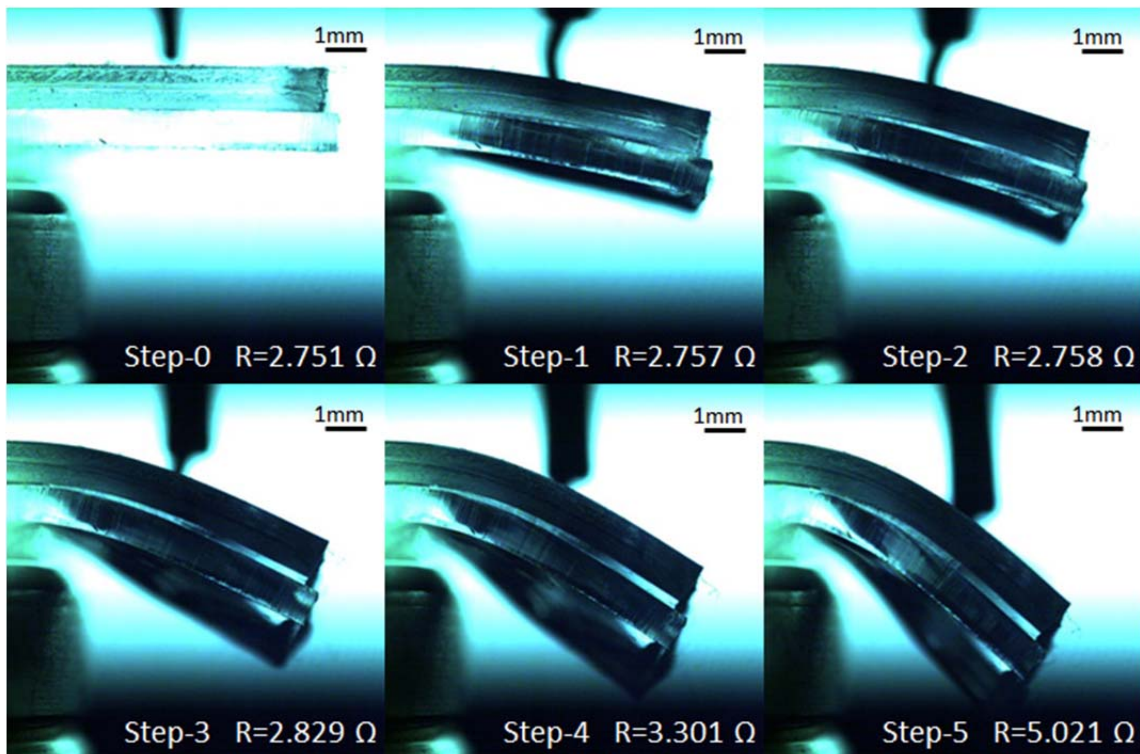

Figure 5.3: The antenna in the mockup device is tested for its electrical conductivity under mechanical stress. The stress is applied in steps while the antenna resistance and the amount of displacement are monitored.

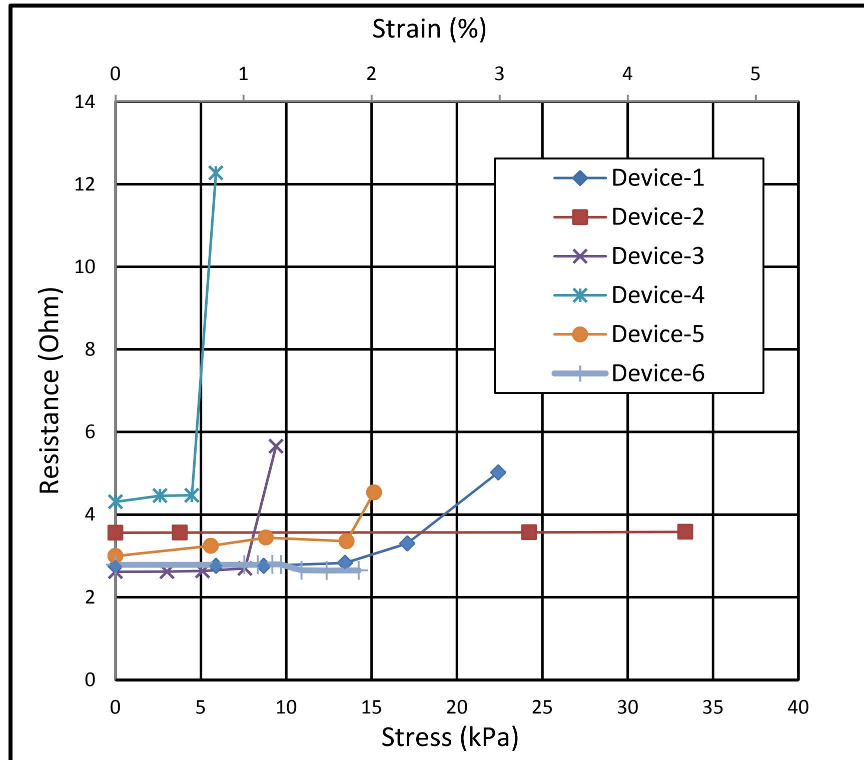

Figure 5.4: Resistance change in solder-filled antenna pattern with applied stress.

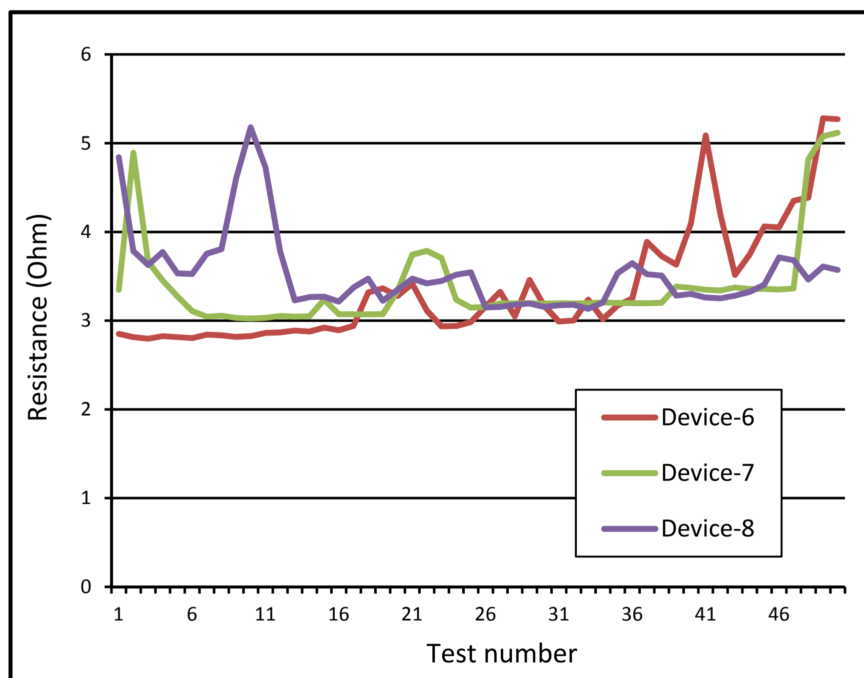

Figure 5.5: The change in antenna resistance after bending the device 50 times.

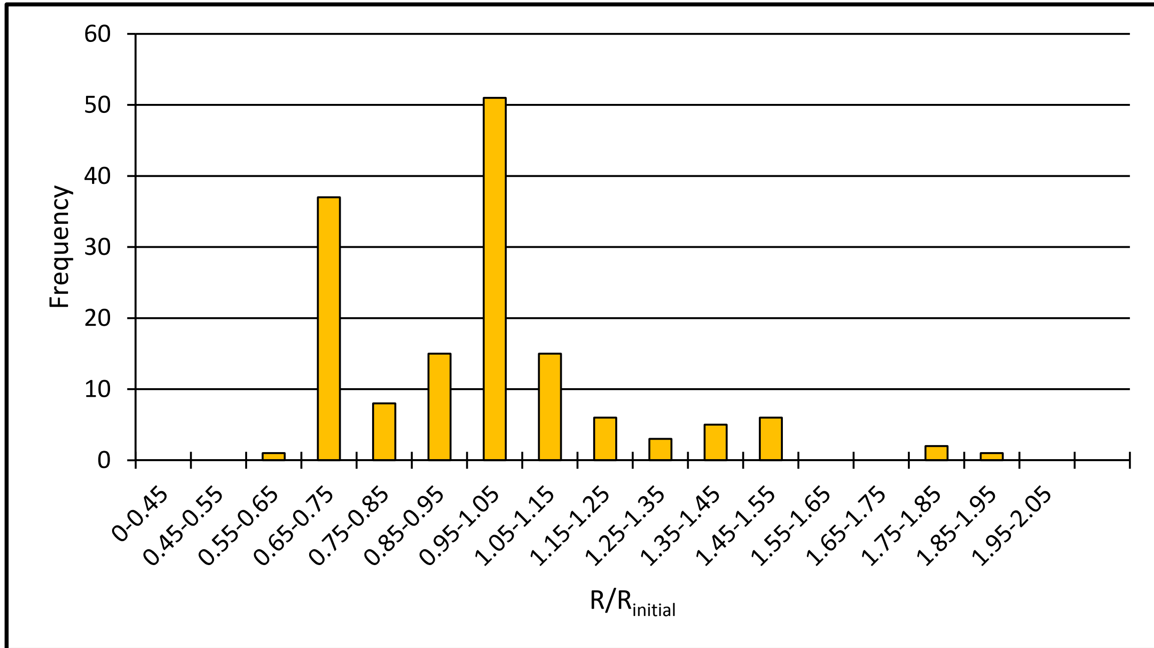

Figure 5.6: Histogram of the antenna resistance measured over 150 bending cycles.

5.5 Conclusion

The IOP monitoring device will go through harsh mechanical conditions during device implantation. Thus, it is important to ensure that the antenna does not lose its electrical conductivity after implantation. Results from the first mechanical test may seem discouraging because of deviation in the maximum applicable stress without disconnecting the antenna. However, the second test shows that there is a tolerable change in the antenna resistance after 50 bending cycles. Since the final implantable device will go through the process of folding and unfolding only once, 50 bending cycles provide enough confidence for its flexibility. The loss of conductivity in the first test can be explained with a weak bond between the SMT component and the antenna. The connection is most likely lost in the SMT-antenna interface due to the weak adhesion between Al connection pads on the SMT and the In/Bi/Sn alloy. The connection is restored due to the mechanical restoring force of the PDMS substrate when the device is relaxed.

The chip used in the final device employs Au electrical connection pads, which have stronger bonding with the metal alloy used for the antenna. A different metal alloy can also be used in the final device if the problem persists. Current tests show that there is no failure of the antenna itself.

CHAPTER 6. PRESSURE MEASUREMENT

6.1 Introduction

The final step in device characterization is pressure sensor testing. This step includes both wired and wireless pressure measurement experiments. The pressure sensor is first tested for the effect of the PDMS coating on sensor reading and sensitivity. Later, the device prototype is used for wireless pressure measurement inside a controlled pressure chamber.

6.2 Effect of PDMS Coating on Pressure Sensor

The effect of PDMS coating on pressure sensor performance is studied before device integration. A Cr/Au metal layer is patterned on a glass substrate with a lift-off process. The capacitive pressure sensor is wire-bonded to the Cr/Au layer. It is placed into a pressure chamber where pressure is varied between 0.3-1 bar. Capacitance is monitored with a Hewlett-Packard 4263A LCR Meter at 100 kHz and 50mV bias. Later, a 50-μm thick PDMS layer is spin-coated on the sensor and cured at 60°C. Sensor response is recorded in the same pressure interval after the spin-coating. The sensor is left to reach a steady state for 5 minutes at each measurement step. The result is plotted with respect to the sensor reading at atmospheric pressure in Figure 6.1. This reference capacitance is 18.28 pF without the PDMS coating and increases to 20.93 pF with the coating. The average sensitivity of the sensor is measured as 0.60 pF/bar initially, increasing to 0.69 pF/bar after the coating. Figure 6.2 presents the amount of change in the sensor capacitance due to the PDMS coating. The maximum change occurs around 0.35 with 0.5%.

The change in capacitance due to the added PDMS mass can be calculated using pressure applied by that mass. It is calculated as 0.47 Pa (4.7×10^{-6} bar) for a 50 μm-thick PDMS layer using equation (6.1). The pressure due to the PDMS coating is insignificant compared to pressure values in the test.

$$P = tdg \tag{6.1}$$

P: pressure

t: thickness of the coating

d: density of the coating

g: gravity

Added PDMS layer does not alter the pressure sensing characteristics. The reason for the slight increase in the sensor capacitance and sensitivity are unknown at this stage. Parasitic charges introduced to the system should be considered.

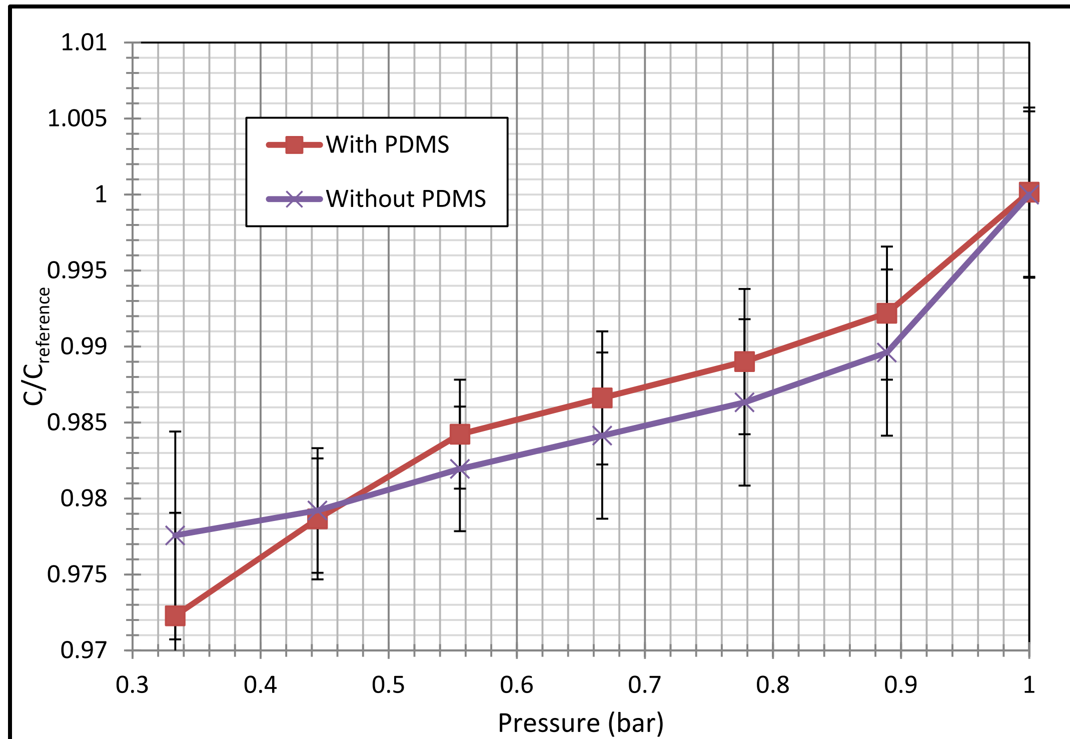

Figure 6.1: Pressure sensor reading before and after PDMS coating. Error bars show the uncertainty in capacitance due to LCR meter.

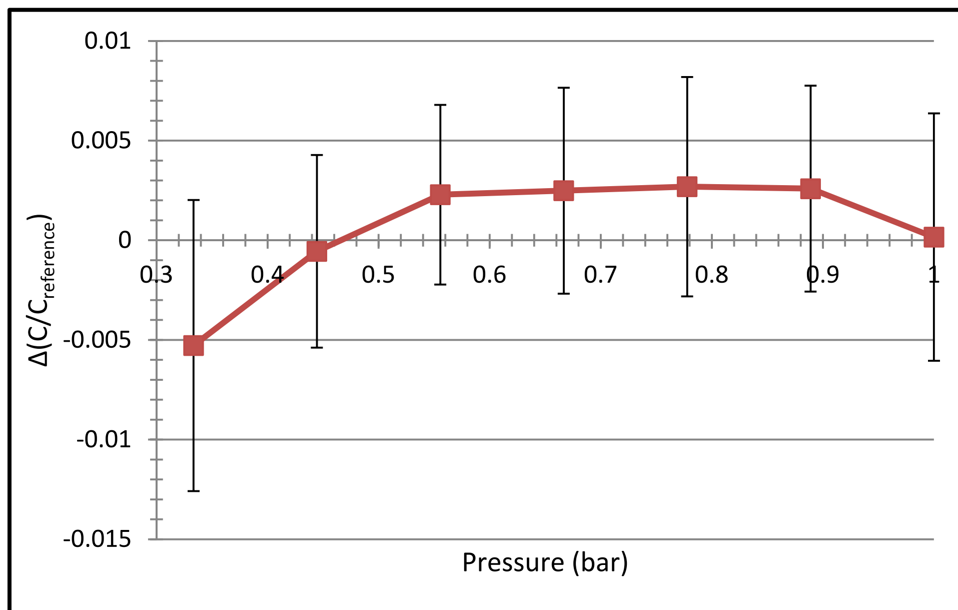

Figure 6.2: Amount of change in pressure sensor capacitance with PDMS coating.

6.3 Wireless Pressure Measurement

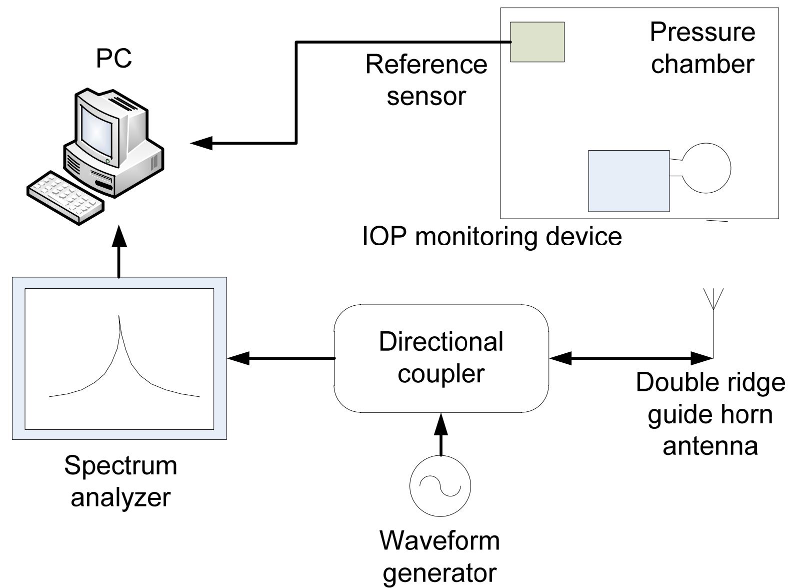

Figure 6.3: Test setup for the wireless pressure measurement.

The setup illustrated in Figure 6.3 is used for wireless pressure measurements from the device prototype. The device is placed in a pressure chamber, which is 1 cm away from the horn antenna. The pressure inside the chamber is controlled by a valve connected to a pressurized air source. The RF signal is transmitted to the device using the RF signal generator (E4438C ESG Vector Signal Generator, Agilent Technologies) and the horn antenna to power the device. The backscattered signal is isolated from the transmitted signal using a directional coupler (Krytar, 4080180) and analyzed with a spectrum analyzer (RSA3408A Real-Time Spectrum Analyzer, Tektronix). A Bosch BMP085 Barometric Pressure Sensor is installed into the pressure chamber as a reference. In each pressure step, the sensor is left to reach a steady state for 5 minutes.

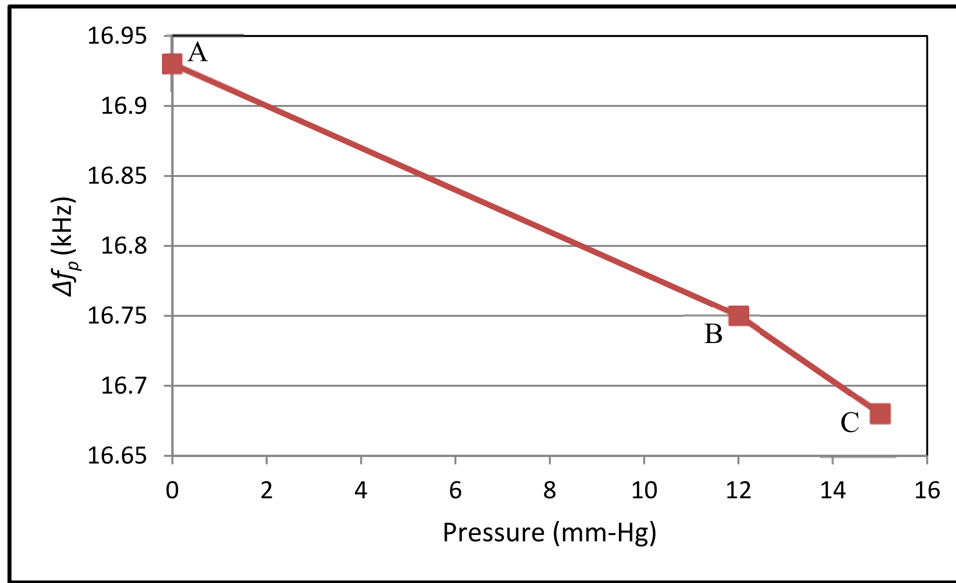

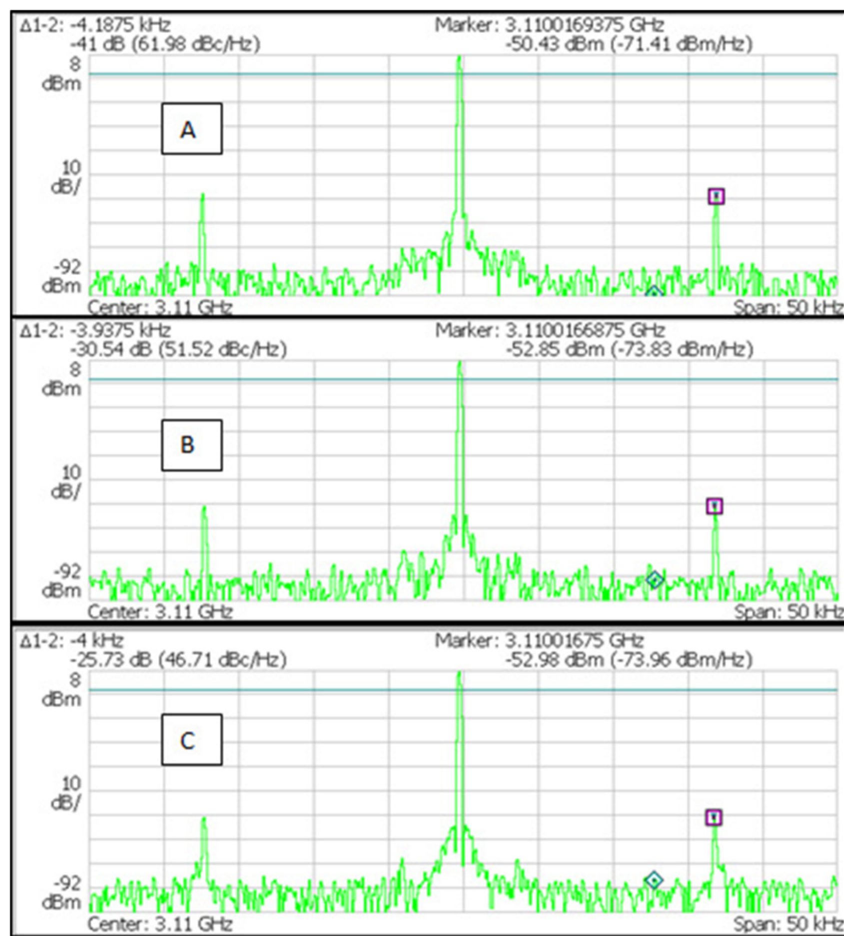

Figure 6.4: Above: Change in Δf_P with increased pressure. Below: Frequency spectrum for each data point.

The RF chip used in the device is operated in reference capacitor transmission mode and pressure transmission mode for the wireless pressure measurement via an I2C connection (Aardvark I2C/SPI Host Adapter, Total Phase Inc.) to the prototype. Two frequency components, carrier frequency (f_{c}) and deviation in frequency due to the measurement result ($\Delta f_{\mathrm{R}}, \Delta f_{\mathrm{P}}$), are observed. The difference between the two frequencies (Δf_{P}) is linearly related to the measured pressure according to equation (6.2) in pressure measurement mode.

$$P = \alpha \frac{\Delta f_{\mathrm{R}}}{\Delta f_{\mathrm{P}}} + P_{\mathrm{o}} \tag{6.2}$$

α: Pressure-frequency shift coefficient

P_{o}: Offset pressure

Δf_{P}, Δf_{R} and pressure from BMP085 is recorded at each measurement step. Results are plotted in Figure 6.4. Δf_{R} is recorded as 12.75 kHz in all steps. α and P_{o} are calculated as –61.32 and 1038.4 after line fitting. Averaged sensitivity is calculated as 16.66 Hz/mm-Hg.

Three data points obtained from the device are encouraging but not enough to claim device operation in the intended pressure interval. Unfortunately, there are several problems observed during the pressure measurement. First of all, the chip is not set to the intended configuration all the time. The operation mode of the chip is decided according to the frequency of the backscattered signal. The configuration bit stream is sent to the device several times before a backscattered signal is obtained. However, it is lost within a few seconds of the RF chip configuration. The signal is restored for another few seconds upon re-sending the chip configuration bit stream. These phenomena are observed consistently in three prototype devices. A writing error in the chip serial interface can explain the observed behavior. A defect or defects in the shift register, either due to the chip fabrication or device integration process, might be the cause. The I2C connection is continuously monitored for signal waveforms and timings of the clock and configuration bit streams to ensure transmission of the correct bit sequence. Board connections and pressure sensor capacitance are also checked to eliminate any failure due to those.

It is observed that the chip is harvesting RF power and temporarily backscattering the measured parameter. The same behavior is also observed in the temperature and reference capacitor modes. Thus, it is concluded to be a configuration interface problem rather than a pressure sensing problem.

6.4 Conclusion

The presented test results show that PDMS coating has a tolerable effect on the capacitive pressure sensing characteristics. It increases the device capacitance as well as sensitivity. However, those changes are relatively small and do not alter the device response. The observed effects can be attributed to the dielectric nature of the coating. It is also seen that the prototype is capable of capturing the pressure information and transmit it to the outside receiver while it is powered wirelessly. However, continuous pressure measurement in the 0-30 mmHg interval is not observed due to the chip configuration problem described in the previous section. Further research is needed to figure out the root-cause of the problem.

CHAPTER 7. CONCLUSIONS AND FUTURE WORK

7.1 Conclusions

The focus of this dissertation is an intraocular pressure monitoring device, which is implanted during cataract surgery. A novel fabrication and packaging method for the monitoring device is introduced. A device prototype is fabricated. Throughout comprehensive modeling and systematic tests, device functionality is demonstrated.

The device illustrated in Figure 2.2 will be embedded in a capsular tension ring like structure in order to be integrated into cataract surgery. Results obtained from three fabrication methods indicate that the solder-filled-microchannel approach is promising for fabrication of the desired IOP sensor as well as other flexible structures. It can fabricate thick metal structures on a flexible substrate without electroplating and at a relatively low process temperature of 75 °C. The presented process achieves the antenna fabrication and the chip integration in a single step. Additionally, heat-assisted repair of broken metal structures is presented.

A device prototype is introduced and fabricated using the solder-filled microchannel process (Figure 3.5). The device is first assembled on a PCB, then successfully embedded into PDMS and integrated with the antenna. The presented method can be used for biocompatible packaging of microsystems and sensors.

The prototype is tested for wireless power and data transfer. Results indicate that it can be powered wirelessly from up to 2 cm distance (Figure 4.2). Calculated electromagnetic power density on the tissue surface is below the maximum permissible exposure limit. Data transfer is proven through the backscattered signal for the programmed chip mode (Figure 4.5). Each mode is clearly visible in the frequency spectrum of the received signal.

Mechanical flexibility of the antenna is tested using a mockup device. Results show that the antenna is conductive up to a mechanical stress of 33 kPa. Connection is lost momentarily at higher stress levels, up to 116 kPa. However, connection is restored upon release of the stress. Test results indicate a tolerable change in the antenna resistance after 50 bending cycles.

The effect of PDMS coating on the pressure sensor is tested. Results show an acceptable increase in capacitance and sensitivity. Wireless pressure measurements are performed with the prototype (Figure 6.4). Results indicate a pressure sensitivity of 16.66 Hz/mm-Hg. However, continuous pressure monitoring in the interval of 0-30 mmHg is not performed due to problems in the chip configuration step.

The prototype presents complete device functionality. Results are promising towards building a complete wireless IOP monitoring device, which can be implanted during a cataract surgery.

7.2 Future Work

7.2.1 Testing in an Eye Model

The effect of environmental variables on device performance should be analyzed. The presented test results show the device functionality in air. However, the device will be implanted into the anterior chamber, in a liquid environment surrounded by layers of tissue. Added layers will cause attenuation in transferred power and received signal levels. The transmitted power level needs to be increased to overcome those while keeping tissue surface radiation below the maximum permissible exposure limit. The amount of attenuation depends on the transmission distance and conductivity of the medium.

Environmental tests can be performed in two steps:

- **Testing in water:** The prototype will be located in a solution similar to aqueous humor in content (mostly water, saline, glucose, proteins, aminoacids, etc.). Wireless power transfer and pressure measurements will be performed.
- **Testing in eye model:** The prototype will be placed into an eye model, which incorporates the fluid in the previous test with a layer of tissue representing the cornea. Wireless power transfer and pressure measurements will be performed.

The antenna design can be changed to improve the antenna gain if transmission problems are observed.

7.2.2 From Prototype to a Complete Device

Operation of the device prototype is presented with systematic testing in this dissertation. Results are encouraging to move from prototyping to a complete device. However, the device size is relatively large due to the PCB. This requires redesign of the RF chip to accommodate the following:

- All SMT components except an SMT capacitor should be removed in the final device.
- The wired connection needed for chip configuration should be removed. Parameters determining the chip operation are configured using a wired connection in the prototype in order to determine the most suitable configuration. Chips can be preset to this configuration during the design. Or, they can be configured wirelessly through an RF signal.

An IOP monitoring device fabricated with the redesigned chip will have a footprint which can be embedded in the capsular tension ring like implant. Thus, in vivo testing will be possible.

7.2.3 Salinity and pH Monitoring

Using an active implanted device also enables monitoring additional health parameters. The

presented prototype can be considered as a platform where monitored parameter or parameters depend on the integrated sensor or sensors. Thus, it can be used for building a battery-less body area network for health monitoring. Bearing that in mind, expansion on the sensing capability should be considered.

Salinity and pH sensors can be added to the prototype in order to observe their effect on IOP and glaucoma. Preliminary studies on salinity and pH measurements are performed using impedance spectrometry. The setup in Figure 7.1 is used for salinity and pH measurements. The electrochemical cell can be modeled using two resistors and a capacitor. When AC voltage at high frequency is applied to the electrochemical cell, the double layer capacitance can be approximated like a short circuit and the resistance of the solution can be measured. This resistance is strongly dependent on the ion concentration in the solution. For the proposed salinity sensor, an AC voltage at 10 kHz is applied to the given electrochemical cell and the current is measured. The resistance is calculated as the ratio of the two values.

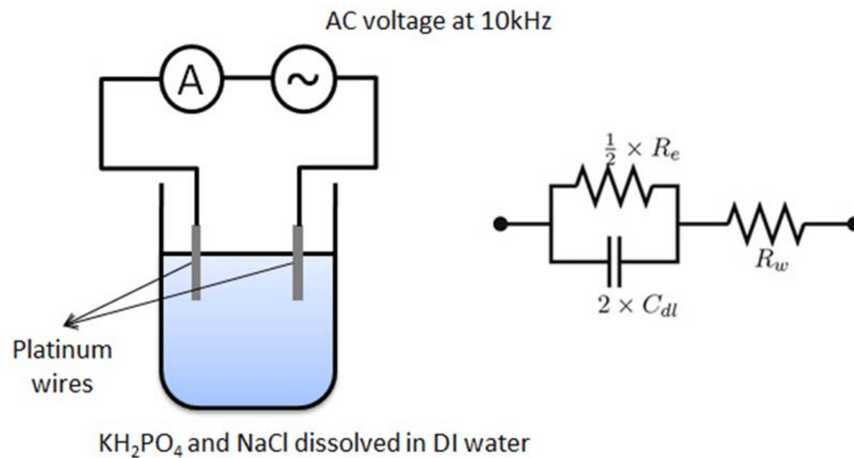

Figure 7.1: Setup used for salinity and pH measurements, and its circuit representation. R_e: resistance due to the redox reactions on the electrodes. R_w: resistance of the solution. C_{dl}: capacitance due to the double layer formation around the electrodes.

Results are plotted in Figure 7.2 and Figure 7.3. Considerable resistance change is obtained with the change in NaCl concentration. However, there is also a strong correlation with pH levels. A measurement method which can isolate pH levels from NaCl concentration should be developed. A drawback of the resistive sensing is an increase in power consumption. That can be prohibitive for limited power budget applications.

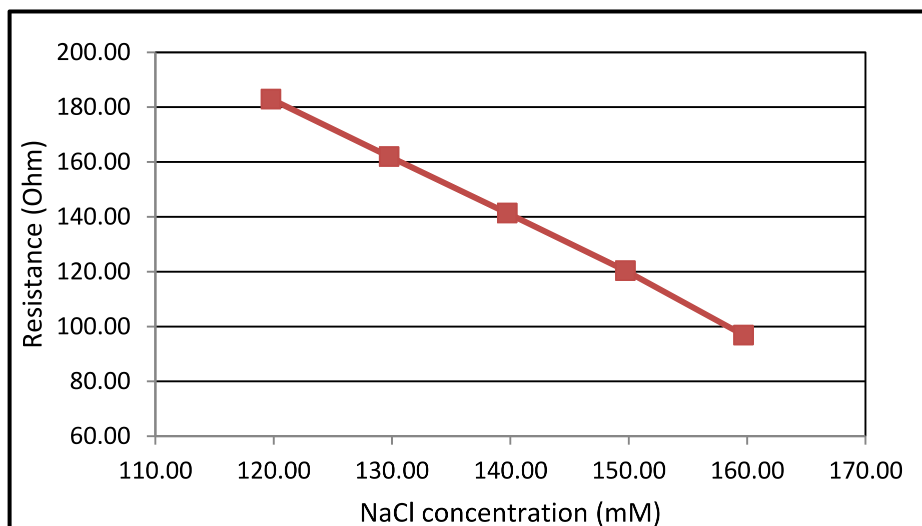

Figure 7.2: Change in solution resistance with NaCl concentration. pH is kept constant in this measurement.

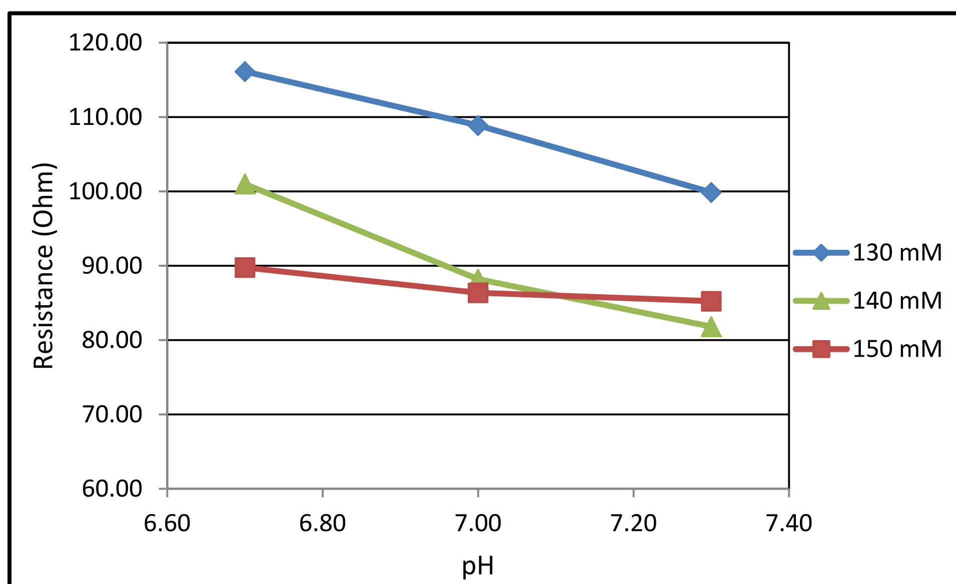

Figure 7.3: Change in solution resistance due to change in pH and NaCl concentration.

A low-power pH and NaCl concentration sensing method needs to be developed. The expansion of platform capabilities can be achieved by the integration of this method into the existing prototype. That may lead to an implanted multi-sensor platform, which can revolutionize the diagnosis tools.

REFERENCES

1. Kingman, S., *Glaucoma is second leading cause of blindness globally.* Bulletin of the World Health Organization, 2004. **82**(11).
2. Quigley, H.A. and A.T. Broman, *The number of people with glaucoma worldwide in 2010 and 2020.* The British Journal of Ophthalmology, 2006. **90**(3): p. 262-7.
3. Hughes, E., P. Spry, and J. Diamond, *24-hour monitoring of intraocular pressure in glaucoma management: a retrospective review.* American Journal of Ophthalmology, 2004. **137**(1).
4. Rosengren, L., et al., *A system for passive implantable pressure sensors.* Sensors and Actuators. A, Physical., 1994. **43**(1/3): p. 55.
5. Schnakenberg, U., et al., *Initial investigations on systems for measuring intraocular pressure.* Sensors and Actuators. A, Physical., 2000. **85**(1): p. 287.
6. Stangel, K., et al., *A programmable intraocular CMOS pressure sensor system implant.* IEEE Journal of Solid-State Circuits, 2001. **36**(7): p. 1094-1100.
7. Chen, P.-J., et al., *Unpowered spiral-tube parylene pressure sensor for intraocular pressure sensing.* Sensors and Actuators A: Physical, 2006. **127**(2): p. 276-282.
8. Chen, P.J., et al., *Microfabricated implantable parylene-based wireless passive intraocular pressure sensors.* Journal of Microelectromechanical Systems, 2008. **17**(6): p. 1342-1351.
9. Haque, R.M. and K.D. Wise. *A 3D implantable microsystem for intraocular pressure monitoring using a glass-in-silicon reflow process*. in IEEE 24th International Conference on Micro Electro Mechanical Systems (MEMS). 2011.
10. Chitnis, G.D., et al. *An ocular tack for minimally invasive continuous wireless monitoring of intraocular pressure*. in IEEE 25th International Conference on Micro Electro Mechanical Systems (MEMS). 2012.
11. Leonardi, M., et al., *First steps toward noninvasive intraocular pressure monitoring with a sensing contact lens.* Invest. Ophthalmol. Vis. Sci., 2004. **45**(9): p. 3113-7.
12. Leonardi, M., et al., *Wireless contact lens sensor for intraocular pressure monitoring: assessment on enucleated pig eyes.* Acta. Ophthalmol, 2009. **87**(4): p. 433-7.
13. Shih, Y.C., B.P. Otis, and T. Shen, *A 2.3 μW wireless intraocular pressure/temperature monitor.* IEEE Journal of Solid-State Circuits, 2011. **46**(11):

p. 2592-2601.

14. Bae, B., et al., *Design optimization of a piezoresistive pressure sensor considering the output signal-to-noise ratio.* Journal of Micromechanics and Microengineering, 2004. **14**(12): p. 1597-1607.
15. Bae, B., K. Park, and M.A. Shannon, *Low-pressure treatment control of glaucoma using an electromagnetic valve actuator with a piezoresistive pressure sensor.* 2005: p. 126-129.
16. Chen, P.J., et al., *Implantable Unpowered Parylene MEMS Intraocular Pressure Sensor*. in International Conference on Microtechnologies in Medicine and Biology. 2006.
17. Chen, P.-J., et al., *Wireless Intraocular Pressure Sensing Using Microfabricated Minimally Invasive Flexible-Coiled LC Sensor Implant.* Journal of Microelectromechanical Systems, 2010. **19**(4).
18. Leonardi, M., et al., *Wireless contact lens sensor for intraocular pressure monitoring: assessment on enucleated pig eyes.* Acta Ophthalmologica, 2009. **87**(4).
19. Stangel, K., et al., *A Programmable Intraocular CMOS Pressure Sensor System Implant.* IEEE Journal of Solid-State Circuits., 2001. **36**(7): p. 1094.
20. Dosso, A.A., et al., *Outcomes of coaxial microincision cataract surgery versus conventional coaxial cataract surgery.* J Cataract Refract. Surg., 2008. **34**(2): p. 284-8.
21. Krupin, T. Feitl, and M.E. Bishop, *Postoperative intraocular pressure rise in open-angle glaucoma patients after cataract or combined cataract-filtration surgery.* OPHTHA Ophthalmology, 1989. **96**(5): p. 579-584.
22. Siegel, A.C., et al., *Cofabrication of electromagnets and microfluidic systems in poly(dimethylsiloxane).* Angewandte Chemie, International Edition, 2006. **45**(41): p. 6877-6882.
23. Siegel, A.C., et al., *Microsolidics: Fabrication of Three-Dimensional Metallic Microstructures in Poly(dimethylsiloxane).* Advanced Materials., 2007. **19**(5): p. 727-733.
24. Siegel, A.C., et al., *Cofabrication: A Strategy for Building Multicomponent Microsystems.* Accounts of Chemical Research, 2010. **43**(4): p. 518-528.
25. Wei, P., et al., *Stretchable microelectrode array using room-temperature liquid alloy interconnects.* Journal of Micromechanics & Microengineering, 2011. **21**(5).
26. Surapaneni, R., et al. *Self-Healing Microfluidic Wires For Ultra-Reliable Flexible Microsystems*. in 15th International Conference on Miniaturized Systems for

Chemistry and Life Sciences. 2011. Seattle, Washington, USA.

27. Armani, D., C. Liu, and N. Aluru. *Re-configurable fluid circuits by PDMS elastomer* in Twelfth IEEE International Conference on micromachining. in Micro Electro Mechanical Systems (MEMS). 1999.
28. Wen, L., et al., *A Parylene temporary packaging technique for MEMS wafer handling.* Sensors & Actuators: A. Physical, 2012. **186**: p. 289-297.
29. Gutierrez, C.A. and E. Meng, *Parylene-based electrochemical-MEMS transducers.* Journal of Microelectromechanical Systems, 2010. **19**(6): p. 1352-1361.
30. Po-Jui, C., et al., *Microfabricated Implantable Parylene-Based Wireless Passive Intraocular Pressure Sensors.* Journal of Microelectromechanical Systems, 2008. **17**(6): p. 1342-1351.
31. Hassler, C., T. Boretius, and T. Stieglitz, *Polymers for neural implants.* Journal of Polymer Science, Part B: Polymer Physics, 2011. **49**(1): p. 18-33.
32. Lago, N., et al., *Long term assessment of axonal regeneration through polyimide regenerative electrodes to interface the peripheral nerve.* Biomaterials., 2005. **26**(14): p. 2021-2031.
33. Richardson, R.R., J.A. Miller, and W.M. Reichert, *Polyimides as biomaterials: preliminary biocompatibility testing.* Biomaterials, 1993. **14**(8): p. 627-635.
34. Jung, I., et al., *Dynamically tunable hemispherical electronic eye camera system with adjustable zoom capability.* Proceedings of the National Academy of Sciences of the United States of America, 2011. **108**(5): p. 1788-1793.
35. Kim, D.-H., et al., *Materials and noncoplanar mesh designs for integrated circuits with linear elastic responses to extreme mechanical deformations.* Proceedings of the National Academy of Sciences of the United States of America., 2008. **105**(48): p. 18675.
36. Sun, Y., et al., *Controlled buckling of semiconductor nanoribbons for stretchable electronics.* Nat Nanotechnol, 2006. **1**(3): p. 201-7.
37. Chang, J.H.C., et al., *High yield packaging for high-density multi-channel chip integration on flexible parylene substrate.* Proceedings of the IEEE International Conference on Micro Electro Mechanical Systems (MEMS), 2012: p. 353-356.
38. Po-Jui, C., et al. *Implantable parylene-based wireless intraocular pressure sensor*. in IEEE 21st International Conference on Micro Electro Mechanical Systems (MEMS). 2008.
39. Po-Jui, C., et al., *Wireless Intraocular Pressure Sensing Using Microfabricated Minimally Invasive Flexible-Coiled LC Sensor Implant.* Journal of

Microelectromechanical Systems, 2010. **19**(4): p. 721-734.
40. Gonenli, I.E., Z. Celik-Butler, and D.P. Butler, *Surface micromachined MEMS accelerometers on flexible polyimide substrate.* IEEE Sensors Journal, 2011. **11**(10): p. 2318-2326.
41. Suh, J.W., et al., *Fully programmable MEMS ciliary actuator arrays formicromanipulation tasks.* Proceedings of the IEEE International Conference on Robotics and Automation , 2000. **2**: p. 1101-1108.
42. Bashir, R., et al., *Micromechanical cantilever as an ultrasensitive pH microsensor.* Applied Physics Letters, 2002. **81**(16): p. 3091.
43. Lee, K.J., K.A. Fosser, and R.G. Nuzzo, *Fabrication of Stable Metallic Patterns Embedded in Poly(dimethylsiloxane) and Model Applications in Non-Planar Electronic and Lab-on-a-Chip Device Patterning.* Advanced Functional Materials., 2005. **15**(4): p. 557.
44. Bowden, N., et al., *Spontaneous formation of ordered structures in thin films of metals supported on an elastomeric polymer.* Nature, 1998. **393**(6681).
45. Chen, X. and J.W. Hutchinson, *Herringbone Buckling Patterns of Compressed Thin Films on Compliant Substrates.* Journal of Applied Mechanics, 2004. **71**(5).
46. Han-Sheng, C. and W. Steven, *Design, fabrication and characterization of a conducting PDMS for microheaters and temperature sensors.* Journal of Micromechanics and Microengineering, 2009. **19**(4).
47. *IEEE Standard for Safety Levels With Respect to Human Exposure to Radio Frequency Electromagnetic Fields, 3 kHz to 300 GHz.* IEEEStd. C95.1, 2006.